Cell-type-resolved *NRXN1* isoforms in human brain and hiPSC cortical organoids

Lei Cao[1*], Yu Fan[1*], Sadaf Ghorbani[2*], Jessica Mariani[2], Yanchun Zhang[1], Michael B. Fernando[3], Jaroslav Bendl[1,4], John Fullard[1,4], Susana Isabel Ramos[5], Edward A. Mead[1], Nicola A.L. Hall[6,7], Gintaras Deikus[1], Kristin G Beaumont[1], Bohan Zhu[1], Sai Ma[1], Robert Sebra[1], Nadejda Tsankova[5], Panos Roussos[1,4,8], Kristen J. Brennand[2#] and Gang Fang[1#]

[1] *Department of Genetics and Genomic Sciences, Icahn School of Medicine at Mount Sinai, New York, NY 10029*
[2] *Department of Psychiatry, Yale School of Medicine, New Haven, CT, 06520*
[3] *Nash Family Department of Neuroscience, Icahn School of Medicine at Mount Sinai, New York, NY, 10029*
[4]*Center for Disease Neurogenomics; & Friedman Brain Institute; & Department of Psychiatry, New York, NY, USA*
[5]*Department of Pathology, Molecular, and Cell-Based Medicine, Icahn School of Medicine at Mount Sinai, New York, NY, 10029, USA*
[6]*Department of Psychiatry, University of Oxford, Warneford Hospital, Oxford, OX3 7JX, UK;*
[7]*Oxford Health NHS Foundation Trust, Warneford Hospital, Oxford, OX3 7JX, UK.*
[8]*Center for Precision Medicine and Translational Therapeutics, Mental Illness Research Education and Clinical Center (MIRECC), James J. Peters VA Medical Center, New York, 10468, USA*
[*]*These authors contributed equally.*

[#]*Correspondence: kristen.brennand@yale.edu, gang.fang@mssm.edu*

ABSTRACT

NRXN1 undergoes extensive alternative splicing that generates a highly diverse repertoire of isoforms, diversifying protein–protein interactions, shaping synaptic specialization, and contributing to neuropsychiatric disease when disrupted. However, the splicing landscape of *NRXN1* across distinct human brain cell types remains poorly defined. Because *NRXN1* expression level is relatively low in adult brains and human induced pluripotent stem cell (hiPSC) derived neurons, single-cell long-read cDNA sequencing often provides insufficient coverage to capture its full isoform diversity, particularly across heterogeneous cell populations. To address this gap, we developed an integrative sequencing strategy that combines single-cell transcriptomics, targeted enrichment of *NRXN1* transcripts, and long-read sequencing. This approach reveals a comprehensive catalog of cell-type resolved *NRXN1* isoforms across adult and fetal human postmortem brains as well as hiPSC-derived cortical organoids. From the adult

prefrontal cortex (PFC) region, our analyses reveal distinct splicing programs across interneuron subtypes, pyramidal neurons, and glial lineages. Comparisons between prenatal and adult brains indicate that *NRXN1* isoform profiles are established during early development and remain stable throughout neuronal maturation. In hiPSC organoid models, splicing profiles partially mirror both developmental and mature brain patterns, with a subset of splice sites exhibiting cell type- and stage-specific divergence. In the cerebellum of an autism case and in organoids derived from schizophrenia patients, carrying non-recurrent heterozygous *NRXN1* deletions, we identify disrupted isoform expression and mutant *NRXN1α* isoforms and characterize their distribution across diverse cell types. Using this integrated long-read sequencing framework in patient-derived organoids, we further show that antisense oligonucleotide (ASO) targeting of mutant splice junctions reduces gain-of-function *NRXN1* isoforms and reshapes splicing patterns in a cell type–specific manner, providing a platform for evaluating ASO efficiency. Together, these findings help understand the cell type–specific splicing landscape of *NRXN1* and establish a framework for decoding cell type-specific isoform diversity and assessing transcript-targeted therapies for genes with low expression levels.

INTRODUCTION

Alternative splicing (AS) is a key post-transcriptional process in the human brain that generates diverse mRNA isoforms, contributing to the brain's functional complexity[1–4]. Presynaptic cell-adhesion molecules known as neurexins (*NRXN1-3*) stand out as canonical examples of AS-driven synaptic diversity, playing central roles in synapse formation, specification, and plasticity[5–9]. The *NRXN1* gene generates an exceptional number of isoforms through six major alternative splice sites (SS1-6)[10–12], which are essential for fine-tuning synaptic properties and diversification. For instance, alternative splicing at splice site 4 (SS4) is known to reshape ligand binding[13–16], while differences at SS3 in hippocampal GABAergic interneurons, specifically parvalbumin-positive (*PV*+) and cholecystokinin-positive (*CCK*+) subtypes, have been linked to distinct presynaptic calcium channel usage and modulatory receptors[17,18]. Aberrant alternative splicing due to *NRXN1*$^{+/-}$ deletions disrupt the excitatory–inhibitory balance by weakening excitatory transmission in glutamatergic neurons and enhancing inhibitory transmission in GABAergic neurons[19], underscoring how precise isoform regulation is critical for maintaining synaptic function.

67 A complete, cell-type-resolved isoform catalog of *NRXN1* remained elusive, particularly due to
68 the technological limitations for detection of the large number of neurexin isoforms and their
69 extensive cellular diversity in the human brain. Methods such as patch pipette-based qPCR[20] and
70 next generation sequencing[20] can examine various insertions at alternatively spliced segments
71 but do not assess the combinatorial nature of splicing events on a single mRNA molecule and
72 lack the throughput to capture the *NRXN1* splicing patterns in large populations of diverse cells.
73 Long-read platforms, coupled with single-cell RNA barcoding, represent a major development to
74 study splicing of complex genes such as *NRXN1* in a cell type-specific manner. However, due to
75 the low expression level of *NRXN1*, these transcriptomic approaches provide insufficient depth to
76 comprehensively assess the large repertoire of *NRXN1* isoforms.

77 To overcome these technical barriers, we developed an integrative sequencing strategy that
78 combines (1) probe-based long-read targeted-seq (long-read Capture-seq)[21,22] with (2) single-
79 cell/single-nucleus RNA isoform sequencing for in-depth *NRXN1* isoform profiling, complemented
80 with (3) an optimized long-read RACE-seq [23,24] (Rapid Amplification of cDNA Ends) based
81 enrichment module to focus on specific mutant isoforms of interest. In the core idea of this
82 integrative strategy, single-cell transcriptomics is used to provide cell-type deconvolution, while
83 targeted capture is used to enrich *NRXN1* transcripts for in-depth analysis; long read sequencing
84 is then employed to achieve the crucial full-length isoform resolution. The use of both probe-based
85 targeting and RACE-seq (PCR-based) enrichment complement each other in recovering the
86 diversity of *NRXN1* isoforms (the strength of probes) and detecting rare or low-abundance mutant
87 isoforms (the strength of RACE-seq). Using this integrative strategy, we mapped a
88 comprehensive catalog of cell-type-specific *NRXN1* isoforms across diverse neuronal and glial
89 populations. From the PFC region of the human adult brain, we revealed distinct splicing profiles
90 across GABAergic interneuron, pyramidal neurons and glial lineages. Interneurons derived from
91 the same developmental origin exhibited similar AS patterns, whereas those derived from different
92 origins showed divergent profiles. Analyses of the AS pattern in fetal brain suggest that *NRXN1*
93 splicing profiles are defined in early development and remain largely consistent during neural
94 maturation. Using hiPSC cortical organoids derived from patients with *NRXN1*$^{+/-}$ deletions and
95 controls, we observed that glial progenitor cells and upper-layer excitatory neurons (Ex-L2/3) are
96 enriched for the mutant isoforms, and we found that the organoids partially recapitulate the
97 *NRXN1* splicing patterns of both developing and adult brains. In the postmortem brain tissue from
98 an autistic patient case carrying a heterozygous *NRXN1* deletion, we found that the mutant
99 isoforms transcribed from deletion allele were enriched in molecular layer interneurons (MLI1/2)

100 and astroglia cells. These findings provide insights into the complex alternative splicing of *NRXN1*
101 across brain cell types, along with a generally applicable framework for decoding cell type-specific
102 isoform diversity for important genes with low gene expression levels.

103

104 RESULTS

105 An integrated strategy reveals a cell-type resolved catalog of *NRXN1* isoforms across 106 human brain and hiPSC cortical organoids

107 Single-cell long-read transcriptomics provides a unique ability to resolve full-length *NRXN1*
108 isoforms across cell types, but whole transcriptomic profiling does not provide sufficient depth of
109 *NRXN1* due to its very low expression level. From the published human postmortem brain single-
110 nuclei Iso-seq data[25], *NRXN1* reads constituted only 0.09-0.2% of the total reads across different
111 cell types, underscoring the need for a targeted enrichment strategy (**Fig. 1a, upper panel**). To
112 maximize isoform recovery while preserving cell-type resolution, we used a targeted sequencing
113 strategy with two complementary components (**Fig. 1b**). To generate a comprehensive isoform
114 catalog, we designed capture probes tiled across all *NRXN1* exons at 1× density, which achieved
115 a ~36-96-fold enrichment of *NRXN1* reads over the non-targeted sequencing method (**Fig. 1a,**
116 **lower panel**). We built on Tequila-seq, which uses isothermal amplification of capture probes
117 from low-cost oligonucleotide templates[21] to reduce per-reaction costs by two to three orders of
118 magnitude while maintaining accurate transcript quantification across gene panels of varying
119 sizes. To recover cell-type specificity for isoforms of interest, particularly the mutant isoforms
120 transcribed from the allele carrying exonic deletions, we adapted the RACE-seq (Rapid
121 Amplification of cDNA Ends) method from short-read and optimized for long-read sequencing to
122 achieve a more sensitive detection of low-abundance isoforms. To link isoforms to specific cell
123 types, we matched the UMIs and cell barcodes on the *NRXN1* reads (from *NRXN1*-targeted long-
124 read sequencing data) with the UMIs from the cell cluster information by short-read single-cell
125 RNA-seq data (**Methods**). This design leveraged the sequencing depth and accuracy of short
126 reads together with full-length isoform resolution by long reads, enabling precise assignment of
127 complex *NRXN1* isoforms to distinct cell types.

128 We applied this workflow to single-cell or single-nucleus cDNA from multiple sources,
129 including the PFC of adult brains, gestational cortical samples and cerebellar tissue from an
130 *NRXN1*$^{+/-}$ autism patient. In addition, cortical organoids derived from schizophrenia patients

131 harboring unique *NRXN1*$^{+/-}$ deletions were profiled to assess the impact of these variants on
132 splicing regulation. After isoform identification and quality filtering, using long-read Capture-seq,
133 we identified 50 distinct *NRXN1* isoforms across all datasets, including 27 previously annotated
134 (five α, five β, five γ, and twelve known others) and 23 novel isoforms not represented in
135 Ensembl[26] (**Extended Fig. 1a**). Cell barcode matching revealed 25 annotated and 19 novel
136 isoforms expressed in glutamatergic and GABAergic neurons across samples (**Fig. 1c**).
137 Expression of these novel isoforms was validated across our in-house datasets and confirmed
138 using independent long-read transcriptomes from postmortem human brains reported by
139 others[25,27] using miniQuant-based quantitative analysis[28] (**Extended Fig. 1b**). Among all the
140 *NRXN1* isoforms, **alpha** isoforms constitute the largest and most structurally complex class. We
141 applied long-read RACE-seq, a more sensitive method to single-cell or single-nucleus cDNA of
142 all samples and identified 103 **alpha** isoforms including 57 that have been reported previously
143 (**Extended Fig. 1c**). We compared exon inclusion across *NRXN1* splice sites (SS1–SS6) in
144 GABAergic and excitatory neurons across all samples and performed PCA. Exons 3 and 4 at SS1
145 and exon 7 at SS2 show consistently higher inclusion in glutamatergic neurons, whereas exon 21
146 at SS4 is enriched in GABAergic neurons in adult PFC. Notably, GABAergic neurons in cortical
147 organoids display a distinct splicing profile driven by exon 23 at SS5 (**Fig. 1d)**.

148 ***NRXN1* exhibits distinct splicing patterns across cell types in adult human brains**

149 To understand *NRXN1* alternative splicing patterns across mature neurons in the human brain,
150 we applied the probe-based long-read Capture-seq on the single-nucleus cDNA from the PFC
151 region of 61 adult donors[27] (**Fig. 2a, b; Extended Fig. 2**). We generated 2.43M *NRXN1* reads,
152 among which 1.13M had 10x single cell barcodes, and 1.03M reads sharing the barcodes with
153 short-read data. By integrating the barcode information from short- and long-read data, a total of
154 125,199 cells were identified across all donors. From the long-read Capture-seq of the single
155 nuclei cDNA pools, we identified 46 isoforms with confident cell barcodes and UMIs matched to
156 short-read data, including 6 alpha isoforms not annotated but reported previously, and 14 isoforms
157 not annotated in Ensembl[26] but later validated by our in-house brain dataset (**Fig. 1c, Extended**
158 **Fig. 1**).

159 The brain comprises a great diversity of cell types, and studying neurons with shared
160 developmental markers offers a means to uncover how *NRXN1* alternative splicing contributes to
161 this cellular and functional diversity. Based on developmental markers[27], neurons were
162 categorized as Neurod2-expressing pyramidal cells[28] (PC), *LHX6*-expressing interneurons[29]

163 (*LHX6*$^+$-INs originated from medial ganglionic eminence, MGE), *PROX1*-expressing
164 interneurons[30] (*PROX1*$^+$-INs originated from caudal ganglionic eminence, CGE), and *LAMP5*$^+$
165 *LHX6*$^+$ GABAergic neurons (*PROX1*$^+$ labeled as *LAMP5*). *LHX6*$^+$-INs can be further subclassified
166 into *PVALB*$^+$ and *SST*$^+$ INs, while *PROX1*$^+$-INs are divided into *LAMP5*$^+$, *SNCG*$^+$, and *VIP*$^+$ INs.
167 GABAergic INs are a highly heterogeneous collection of cell types, characterized by their unique
168 spatial and temporal capabilities to influence neuronal circuits[31–33]. We observed that GABAergic
169 interneurons showed the greatest *NRXN1* splicing diversity (**Fig. 2c, top**). Splicing patterns were
170 more variable at SS1, SS3, and SS4, whereas SS2 and SS6 were invariably excluded and SS5
171 was consistently included. Within the *PROX1*$^+$-INs, *the LAMP5*$^+$*, SNCG*$^+$ and *VIP*$^+$ subtypes share
172 similar patterns across all 6 alternative splicing sites, while *PVALB*$^+$ and *SST*$^+$, subclasses of
173 *LHX6*$^+$-INs, differed at SS1. We also identified a *LAMP5*$^+$ *LHX6*$^+$ subclass that shared splicing
174 patterns with the *PROX1*$^+$-INs and *SST*$^+$ of *LHX6*$^+$- INs (**Fig. 2c**). In PC neurons (**Fig. 2c, middle**),
175 we found: (1) across cortical layers, exons at SS1, SS3 and SS5 were dominantly spliced in ("in";
176 upward bars), while exons at ASS6 and SS4 are dominantly spliced out; (2) layer-specific
177 differences at SS2, where exon 7 was often spliced out in PCs of layers L2/3-IT, L5-IT, and L6-
178 IT-Car3, but spliced-in into most PCs of layers L4-IT, L5/6-NP, L6B, L6-CT, and L6-IT. Among
179 glial cells (astrocytes, oligodendrocyte progenitor cells (OPCs), oligodendrocytes), exon 17 at
180 SS6 was consistently spliced out, whereas exon 23 at SS5 was spliced in. Oligodendrocytes
181 showed spliced-in for exon1 and exon5 at SS1, which were dominantly spliced-out in astrocytes
182 and OPCs. At ASS4, exon 21 was included in astrocytes but not in OPCs or oligodendrocytes,
183 consistent with prior studies showing that astrocytic neurexins splice SS4 at high ratios compared
184 to excitatory neuronal neurexins[34,35].

185 Building on the striking patterns of *NRXN1* alternative splicing observed in the human
186 brain, we conducted principal component analysis (PCA) of splicing levels across cell types, which
187 separately clustered *PROX1*$^+$-INs, *LHX6*$^+$-INs and PCs classes (**Fig. 2d**). To identify *NRXN1*
188 splicing events distinguishing glutamatergic (Glu; n = 9) and GABAergic (GABA; n = 4) neurons,
189 we compared mean exon inclusion across 6 splice-site events using Welch's t-tests with
190 Benjamini–Hochberg correction. SS2-7 and SS3-12 exhibited higher inclusion in Glu neurons,
191 whereas SS4-21 was preferentially included in GABA neurons (**Fig. 2e**). Overall, these findings
192 suggest that *NRXN1* splicing profiles exhibit substantial differences across various neuronal
193 populations and glial lineages. Within GABAergic neurons, interneurons derived from the CGE
194 (*PROX1*$^+$-INs subtypes) are closely clustered by the splicing patterns, yet different from INs
195 originating from the MGE (*LHX6*$^+$-INs subtypes).

196 ***NRXN1* splicing profiles are conserved between fetal and adult neurons within**
197 **defined neurogenic lineages**

198 To determine whether the *NRXN1* splicing patterns of the adult brain are defined as early as in
199 the human developing neocortex, we generated a snRNA-seq dataset from two unfixed snap-
200 frozen postmortem neocortex samples obtained from the second and third trimesters of gestation
201 (24 and 33 gestational weeks, gw). After quality control, we obtained the transcriptomic profile of
202 52,426 nuclei, with a median of 2,910 genes, 6,156 UMIs from each nucleus. We identified 10
203 primary cell types from the single cell transcriptome: five neuronal clusters, including excitatory
204 neuronal subpopulations expressing layer-specific cortical marker genes (EX-L2/3, EX-L4/5/6);
205 inhibitory neuronal subpopulations (IN-CGE, IN-MGE and IN-Reelin); and glial cell populations,
206 radial glia and astrocyte (RG/AC) clusters, astrocytes, OPCs, transient glial intermediate
207 progenitor cell (gIPC) population, microglia and *FLT1*+ blood vessel cells (BVCs)[36] (**Fig. 3a**). We
208 further validated our cell annotations by comparing top differentially expressed genes (DEGs) per
209 cell cluster to published canonical lineage and proliferation markers[36,37] (**Fig. 3c, Supplementary**
210 **Table 3**). Next, we analyzed how cell type proportion varied between prenatal neocortex and adult
211 PFC. The 33 gw neocortex sample had more glial, INs-MGE and INs-CGE, whereas the 23 gw
212 sample had more INs-Reelin and excitatory neurons EX-L4/5/6 (**Fig. 3b**). Neuronal populations
213 constituted most cells in the fetal neocortex, whereas glial transient intermediate progenitor cells
214 were exclusively present in fetal neocortex and subsequently disappeared or transformed along
215 with the cortical development in adult PFC, which is consistent with the stages of neurogenesis
216 in human cerebral cortex[38,39] (**Extended Fig.3**).

217 To determine *NRXN1* splicing patterns by cell type in the fetal neocortex, we applied the
218 probe-based long-read Capture-seq on the single nuclei cDNA. Based on regional marker genes,
219 exon 23 at SS5 was predominantly spliced-in across all cell types, whereas exons at other splice
220 sites showed variable inclusion. In most (>60%) PCs across all layers, exons at SS1 and SS3
221 were consistently spliced in, exon 21 at SS4 was spliced out, and exon 17 at SS6 showed variable
222 usage. In contrast, exon 7 at SS2 was differentially spliced between upper-layer (L2/3) and
223 deeper-layer (L4/5/6) PCs. Similarly, in GABAergic interneurons (INs), exons at SS1 and SS3
224 were largely spliced in, while exons at SS2, SS4, and SS6 were spliced out. Notably, the
225 proportion of IN-*LHX6*$^{+}$ cells was higher than that of IN-*PROX1*$^{+}$ cells at SS3 (spliced in) and SS4
226 (spliced out). The glial cells were variably spliced at SS1, SS2, SS6 and SS4, but consistently
227 spliced-in at SS3 and SS5 (**Fig. 3d**). We next compared *NRXN1* splicing in matched neuronal
228 populations between prenatal neocortex and adult PFC. Exon inclusion level across 6 splicing

229 sites were highly correlated between prenatal neocortex and adult PFC for *LHX6*$^{+}$-INs (*Pearson's*
230 *r* = 0.82, *p* = 0.01), *PROX1*$^{+}$-INs (*Pearson's r* = 0.87, *p* = 0.005), PCs (*Pearson's r* = 0.87, *p* =
231 0.005) and glial populations (OPC, *Pearson's r* = 0.9, *p* = 0.003; RG/AC, *Pearson's r* = 0.82, *p* =
232 0.01) (**Fig. 3e, Extended Fig. 3**). These findings suggest that *NRXN1* splicing profiles are defined
233 in early development and remain largely consistent during neural maturation.

234 ***NRXN1*$^{+/-}$ splicing profiles in human cortical organoids recapitulate developmental and**
235 **mature features and identify cell types expressing the mutant isoforms.**

236 From hiPSC-derived two-dimensional (2D) neurons with a 3′-*NRXN1* deletion, we previously
237 uncovered dozens of mutant isoforms exclusively from the deletion-carrying allele (mainly
238 affecting alpha and beta isoforms)[12]. Later, we demonstrated that this exonic deletions at the 3'
239 site disrupted normal *NRXN1* splicing and isoform expression, leading to distinct phenotypes in
240 induced glutamatergic (iGLUTs) and GABAergic (iGABAs) neurons, primarily reflected in
241 altered synaptic frequency[19,40]. Building on these observations, we sought to explore how the
242 deletions affect the splicing events across cell types in a more complex neurodevelopmental
243 system. We generated human cortical organoids (hCOs) from a control line and schizophrenia
244 probands with the 3'deletion (3'-del) in parallel. hCOs were guided toward the forebrain[41]
245 (**Methods, Extended Fig. 4**). To profile cell types in the hCOs, we performed single cell RNA-
246 seq on hCOs from two 3'-del cases (line 581 and line 641) and one control line (line 690) at day
247 150 with the 10x NextGEM 5pv2 kit, when neural activity is well characterized[42–44]. After quality
248 control data processing steps, we merged high-quality scRNA-seq data from 3 cortical organoid
249 samples into a core dataset of 27,325 cells. Following unsupervised clustering, we identified and
250 annotated major cell types using an extensive curated list of known marker genes[19,41], which
251 consisted of transit-amplifying cell (TAC), neuronal intermediate progenitor cells (nIPCs) giving
252 rise to distinct subpopulations of glutamatergic excitatory neurons (Ex-L2/3, Ex-L4/5/6) and
253 GABAergic inhibitory neurons (INs, IN-*SST*,IN-Reelin); gIPCs leading to the subpopulations of
254 radial glia and astrocyte clusters (RG/AC); as well as BVCs (**Fig. 4a**). We further validated our
255 cell annotations by comparing gene expression signatures of our scRNAseq cell clusters to
256 published brain organoid datasets as reference (**Fig. 4b, Supplementary Table 4**). We then
257 compared cortical organoids derived from the control hiPSC line with the prenatal neocortex in
258 terms of cell-type composition. We found gIPCs (OR = 2.06, *Fisher's test*) and Ex-L2/3 (OR =
259 1.67, *Fisher's test*) were significantly enriched in hCOs from the 3'-del lines than in control lines,
260 while cell number of IN-Reelin were significantly low in 3'-del lines (OR = 0.03, *Fisher's test*) (**Fig.**
261 **4c**).

262 To better understand the greater splicing patterns of *NRXN1* across cortical organoid cell
263 types, we applied the long-read Capture-seq on the full-length single-cell cDNA. From the control
264 lines and those with the 3'-deletion, we generated 317,521 *NRXN1* reads, of which 144,450 with
265 10x single cell barcodes and 120,873 reads sharing the barcodes with short-read data. Integrating
266 the barcode information across short- and long-read data, we identified 23,187 cells from all
267 cortical organoid samples (**Extended Fig. 4**). Using these targeted single cell data, we first
268 analyzed the *NRXN1* AS patterns in excitatory neurons, inhibitory neurons and non-neuronal cells
269 for both 3'-del lines and control lines at the advanced maturation stage. Within the glutamatergic
270 excitatory neurons (the major population in hCOs), *NRXN1* splicing patterns were highly similar
271 between the control line and 3'del lines, except for differences in exon inclusion level at SS1 (exon
272 3) and SS3 (exon 12) (**Fig. 4d,e**). The ~136-kb deletion impacting SS4 and SS5 (exons 21-23)[12,19]
273 slightly reduced exon inclusion at SS4 in the 3'-del lines (**Fig. 4e**).

274 As the deletion in the 3'-region of *NRXN1* generates mutant alpha and mutant beta
275 isoforms, we sought to dissect which cell types are enriched for these mutant isoforms. As some
276 of the mutant isoforms are low in abundance and the long-read Capture-seq works better with
277 abundant isoforms,-we employed long-read 5'RACE-seq to resolve alpha isoforms with single cell
278 barcode information from the 5'GEX single cell cDNA (Methods). We identified 21 α-isoforms
279 across all cortical organoids, of which 18 were not detected by long-read Capture-seq, including
280 six mutant isoforms from the two 3′-del *NRXN1*$^{+/-}$ derived organoids (**Fig. 4f**). In addition, we
281 identified seven β-isoforms, including one mutant β-isoform (**Extended Fig. 4**). Compared with
282 the control line, the mutant α-isoforms were expressed widely across all cell types in both lines
283 with 3′-*NRXN1*$^{+/-}$ (except for *DLX1/2*-INs in 641). In contrast, the mutant β-isoform was detected
284 in fewer cell clusters, showing consistent expression in excitatory neurons in both 3′-*NRXN1*$^{+/-}$
285 lines, and exclusively in TACs in line 581 and RG/AC cells in line 641 (**Fig. 4g**). The composition
286 of *NRXN1* isoform by cell type demonstrated that mutant isoforms from the allele bearing 3'-
287 deletion are expressed in all cell types, contributing to altered synaptic activity in excitatory
288 neurons and *DLX1/2*-INs.

289 With *NRXN1* splicing profiles available across multiple developmental stages, we next
290 asked which stage the control hCOs most closely resemble in terms of *NRXN1* splicing– the fetal
291 neocortex or the adult PFC. We therefore compared the exon inclusion level across splicing sites
292 (SS1-6) for *NRXN1* in three major cell classes that appear in all samples, *i.e.,* GABAergic
293 inhibitory neurons, excitatory neurons, and RG/AC (**Fig. 4h**). In GABAergic neurons, exon
294 inclusion levels were highly correlated between organoids and the fetal neocortex (Pearson's r =

295 *0.97, p = 3.82E-04*) and between cortical organoids and the adult PFC (Pearson's *r = 0.88, p =*
296 *0.008*), although exons at SS2, SS3, and SS5 displayed differential splicing. Similarly, significant
297 agreement was observed between cortical organoids and the fetal neocortex in glutamatergic
298 excitatory (Glu-EX; *Pearson's r = 0.73, p = 0.04*) and radial glia/astrocyte (RG/AC; Pearson's *r =*
299 *0.78, p = 0.04*) populations, and between organoids and the adult PFC in Glu-EX (Pearson's *r =*
300 *0.88, p = 0.004*) and RG/AC (Pearson's *r = 0.92, p = 0.003*) populations (**Extended Fig. 4**).
301 Together, these findings indicate that cortical organoid splicing profiles partially recapitulate both
302 developmental and mature splicing patterns, with a subset of splice sites showing cell type- and
303 stage-specific divergence (**Fig. 4h, Extended Fig. 4**).

304 **Mutant *NRXN1* isoforms are enriched in MLIs in ASD cerebellum with *exonic* deletion**

305 *NRXN1* deletions are also strong risk factors for autism spectrum disorder (ASD)[45,46]. The
306 cerebellum shows consistent structural and functional alterations in ASD, and *NRXN1α* isoform
307 complexity is significantly different in the cerebellum compared to the cerebral cortex. To
308 understand *NRXN1* isoform diversity in human brain with *NRXN1* heterozygous deletion, we
309 applied our probe-based long-read Capture-seq to the postmortem cerebellum of an ASD patient
310 with $NRXN1^{+/-}$ (encompassing exon 9-13) (**Extended Fig. 5a**). We performed single-nucleus
311 RNA-seq on this sample and obtained 9,689 high-quality nuclei. Unsupervised clustering and
312 annotation identified eight cerebellar cell type classes: excitatory granule cells; inhibitory neurons
313 (Purkinje cells; two types of molecular layer interneurons MLI1, MLI2; and Purkinje-layer
314 interneurons); astrocytes; Bergmann glia; oligodendrocytes; and OPCs (**Fig. 5a**). These
315 annotations matched expected marker gene expression[47] (**Extended Fig. 5b, Supplementary**
316 **Table 5**).

317 When applying the probe-based long-read Capture-seq to the single nuclei cDNA of the
318 cerebellum, we identified 9 *NRXN1* isoforms with cell barcodes matched to short-read data,
319 including two mutant isoforms associated with the exon 9-13 deletion (**Fig. 5b,c)**. Among *NRXN1*
320 reads with cell barcodes matched to short-read data, the mutant isoforms 3312 and 4131 were
321 exclusively detected in *NRXN1*-deletion cerebellum, with transcript 3312 being the most abundant
322 and 4131 less abundant, together accounting for 28.34% of reads (**Fig. 5c**). When assigning
323 isoforms to cell types, we found the two mutant isoforms were significantly enriched in MLI1
324 (Fisher's Exact test, *p* =5.72E-18), MLI2 (Fisher's Exact test, *p* =0.04), and astroglia cells (Fisher's
325 Exact test, *p* =51.49E-13) compared to wild-type *NRXN1* isoforms (**Fig. 5d**). The enrichment of
326 mutant isoforms in MLIs, key GABAergic regulators of Purkinje cell output, links these mutations

327 to ASD-associated E/I imbalance, suggesting impaired inhibitory circuitry as a primary site of
328 cerebellar vulnerability[48–50].

329 Next, we examined *NRXN1* splicing across six alternative splice sites in these cell types.
330 In the ASD case with *NRXN1* deletion, more than 70% of granule cells showed exon inclusion at
331 SS1, SS3, SS4, and SS5, with moderate inclusion at SS2 (>50%) and predominant exon
332 exclusion at SS6. The two MLI subtypes exhibited distinct splicing patterns, particularly at SS1
333 and SS2. In controls, *NRXN1* splicing varied across cell types, most prominently at SS2–SS4.
334 Comparative analysis revealed broadly similar splicing patterns between ASD and control in
335 granule cells and MLI1 cells, with high exon inclusion at SS1, SS3, SS4, and SS5, variable
336 inclusion at SS2, and predominant exclusion at SS6. In contrast, subtype-specific differences
337 were observed in MLI2 cells (SS1 and SS2), PLI cells (SS3), and Purkinje cells (SS4) (**Fig. 5e,**
338 **Extended Fig. 5c**).

339 To gain insight into how exonic deletion of *NRXN1* affects the DEG networks in the
340 cerebellum potentially associated with ASD, we performed differential expression (DE) analysis
341 for each cell type between control and *NRXN1*-del (see Materials and Methods for details). we
342 then performed Gene Ontology analysis on the up- and downregulated genes per cell type and
343 grouped significantly enriched terms into 20 biological themes (**Extended Fig. 5d**,
344 **Supplementary Table 6,7**). Biological themes related to synapse organization and neuron
345 projection development were associated with DEG sets within excitatory and inhibitory neuronal
346 populations (**Fig. 5f**). Given the prevalence of pathways related to synaptic structure and function,
347 we further assessed enrichment of synaptic compartment genes using the SynGO database. The
348 top-level SynGO category "synapse" was significantly enriched (FDR < 0.05, Hypergeometric
349 test) across all neuronal cell types (**Fig. 5g**).

350 Cell-type–resolved evaluation of ASO inhibition of GOF *NRXN1* isoforms in cortical
351 organoids

352 Antisense oligonucleotides (ASOs), recently used to treat several neurological diseases[51], provide
353 a strategy to selectively target disease-associated mutant isoforms by modulating specific RNA
354 splice sites. In our recent work, we tested ASO efficacy in 2D iGLUT neurons with bulk RNA-seq,
355 but this approach lacked cellular complexity and cell-type resolution[19]. We hypothesized that ASO
356 efficacy and impact are cell-type specific, particularly in inhibitory neuronal populations enriched
357 for mutant isoforms. Here, we applied the long-read single cell targeted-seq approach to evaluate
358 ASO in three-dimensional (3D) human cortical organoids in a cell type–resolved manner. We

359 adopted the same ASO design that target the exon 20–24 mutant splice junction and applied ASO
360 treatment (10 μM) to the organoids derived from 641 line (3'-del) for 96 hours (see Methods;
361 Extended Fig. 6a, b). We collected the ASO-treated organoids for single-cell cDNA synthesis,
362 using half of the single-cell cDNA for *NRXN1* isoform profiling with both 5'RACR-seq and long-
363 read Capture-seq, while the other half used for cell type annotation by single-cell RNA-seq. From
364 the NRXN1-targeted long-read sequencing data, we found ASO-Aplus decreased total NRXN1-
365 MT isoforms by approximately 51% in all cells (**Extended Fig. 6b,c**). Differential splicing
366 analysis confirmed a reduction in GOF splicing (**Fig. 6a**, ΔPSI (percent spliced index) =
367 −0.23), increased exon23 inclusion at SS5 (ΔPSI = 0.313) and decreased exon 21
368 inclusion at SS4 (ΔPSI = −0.154), accompanied by a significant shift from α to β isoforms
369 (**Extended Fig. 6c**, $p < 0.001$, Fisher's exact test).

370 To understand which cell types are mostly perturbed by ASO targeting of the mutant
371 isoforms in the hCOs, we first analyzed single-cell data from the ASO-treated organoids for cell
372 type annotation (**Fig. 6b**, **Extended Fig. 6d**). We did not observe significant difference for cell
373 composition between the organoids treated with ASO-NT and ASO-Aplus (**Fig. 6b**). Single-cell
374 RNA-seq profiling revealed robust downregulated DEGs in IN and RG/AC cells after ASO-Aplus
375 treatment, enriched for regulation of translation and RNA splicing reported by previous study[52]
376 (**Extended Fig. 6e,f** and **Supplementary Table 8**).

377 Integration with cell type–resolved single-cell RNA-seq data revealed that the proportion
378 of *NRXN1* reads containing exons 20–24 was markedly reduced in RG/AC cells and IN cells
379 following ASO-Aplus treatment (**Fig. 6c**). Most importantly, ASO-Aplus significantly reduced
380 proportion of *NRXN1*-MT reads in nIPCs (**Fig. 6d**; OR = 0.015, $p = 1.53 \times 10^{-7}$, BH-adjusted $p =$
381 6.13×10^{-7}, Fisher's Exact test) and showed decreased trend in excitatory neurons, not in RG/AC,
382 indicating cell-type–specific differences in the uptake efficiency of ASOs delivered via gymnosis
383 and/or their knockdown efficacy within each cell type. The activity of ASO-Aplus is consistent with
384 established cell-type differences in ASO efficacy in the central nervous system, where neuronal
385 populations show greater target engagement and higher transfection[53,54]. The decreased
386 proportion of RG/AC in ASO-treated conditions without accompanying *NRXN1*-MT knockdown in
387 those cells suggests a selective cytotoxic or antiproliferative effect on RG/AC rather than on-target
388 silencing[55]. Splicing analysis revealed that exon 21 (SS4) was reversely spliced across all cell
389 types, whereas exon 23 (SS5) remained consistently included following ASO-Aplus compared to
390 ASO-NT treatment. In RG/AC cells, exons at SS1, SS3, and SS4 also exhibited reversed splicing,

391 while splicing patterns at SS2, SS5, and SS6 were largely unchanged between ASO-Aplus and
392 ASO-NT conditions (**Fig. 6e**). Notably, neither wild-type transcripts containing exons 20–24 nor
393 the mutant were detected in INs (**Fig. 6c**). This likely reflects partial overlap of the ASO-Aplus
394 sequence with exons 20 and 24, resulting in unintended targeting of wild-type *NRXN1* in addition
395 to *NRXN1*-MT derived from the 3′ deletion allele (**Extended Fig. 6b**).

396 Altogether, we characterized alterations in MT vs WT *NRXN1* transcripts and splicing
397 events across cell types following ASO treatment using long-read Capture-seq and long-read
398 RACE-seq in hCOs derived from a 3′-del patient. These results highlight the combined use of
399 long-read Capture-seq and RACE-seq as a powerful toolkit for comprehensive evaluation of ASO-
400 induced changes in transcript repertoires and splicing patterns across diverse cell types.

401

402 # DISCUSSION

403 We applied an integrative isoform sequencing strategy combining long-read Capture-seq and
404 long-read RACE-seq to generate a cell-type–resolved catalog of *NRXN1* isoform diversity across
405 human cortical organoids, prenatal cortex, adult PFC, and cerebellum. *NRXN1* exhibited
406 pronounced cell type– and subtype-specific splicing patterns. In human cortical organoids and
407 adult PFC, *NRXN1* splicing showed clear cell-type specificity, whereas analysis of cerebellar
408 tissue from an ASD case revealed deletion-associated isoforms enriched in molecular-layer
409 interneurons and astroglia. Using this framework, we further demonstrated that ASOs targeting
410 the mutant splice junction promote degradation of mutant isoforms in specific cell types within
411 patient-derived organoids. Together, these results establish a platform for resolving *NRXN1*
412 alternative splicing at cell-type resolution and for evaluating ASO-mediated transcript
413 perturbations across cellular contexts.

414 Our strategy integrates probe-based enrichment, single-cell barcoding, and long-read
415 sequencing to overcome key challenges in detecting low-abundance, full-length *NRXN1*
416 transcripts. Targeted capture increased on-target recovery by approximately 50-fold compared
417 with untargeted long-read approaches while preserving single-cell resolution. This workflow links
418 full-length isoforms to their cellular identities, enabling quantitative mapping of *NRXN1* splicing
419 across neuronal and glial populations and connecting genetic variation to functional transcriptomic
420 phenotypes.

421 Glutamatergic neurons, the predominant cortical population, demonstrated highly
422 concordant of *NRXN1* splicing patterns between prenatal neocortex and adult PFC. Likewise,
423 glutamatergic neurons in iPSC-derived cortical organoids recapitulated splicing profiles observed
424 in the prenatal cortex, suggesting that *NRXN1*$^{+/-}$ organoids capture key developmental splicing
425 programs. GABAergic interneurons in the PFC exhibited substantial molecular diversity, reflected
426 in distinct *NRXN1* splicing patterns. Although *PVALB*-expressing and *SST*-expressing
427 interneurons both originate from the MGE (*LHX6*+), they showed subtype-specific exon usage
428 consistent with their known functional divergence[56,57]. Notably, *NRXN1* splicing programs appear
429 to be established early in development and remain largely stable, as evidenced by the strong
430 concordance of exon inclusion levels in *PROX1*$^{+}$ interneurons between the prenatal neocortex
431 and adult PFC[20].

432 Analysis of an *NRXN1*$^{+/-}$ cerebellum from an ASD patient revealed unique mutant isoforms
433 carrying an exon 9–13 deletion that were enriched in molecular-layer interneurons and astroglia,
434 whereas granule cells predominantly expressed wild-type isoforms. Compared to a neurotypical
435 cerebellum, *NRXN1* intergenic deletion was associated with cell-type–specific alterations in gene
436 expression networks. Notably, pathways related to synapse organization and neuron projection
437 development were enriched in both excitatory and inhibitory neuronal populations. Consistent with
438 this, SynGO analysis showed significant enrichment of synaptic compartment genes across all
439 neuronal cell types, indicating convergent disruptions in synaptic structure and function. [13,59]These
440 findings support previous reports that *NRXN1* deletions perturb cortical and cerebellar circuits
441 through cell-type–specific mechanisms, consistent with circuit dysfunction observed in ASD and
442 schizophrenia[58–60]. Given that *NRXN1* isoforms determine synaptic partner specificity, the isoform
443 atlas generated here provides a foundation for isoform-targeted therapeutic strategies, including
444 ASO-based modulation of pathogenic splicing.

445 Long-read Capture-seq and RACE-seq provide complementary approaches for transcript
446 isoform characterization. Capture-seq uses probe-based enrichment of single-cell barcoded
447 cDNA[61] to detect diverse isoforms, including alternative transcription start and termination sites,
448 across multiple cell types while preserving relative transcript abundance. However, this method
449 preferentially captures abundant transcripts and shows reduced sensitivity for low-abundance or
450 long α-isoforms. In contrast, RACE-seq selectively amplifies transcripts from defined 5′ or 3′ ends,
451 enabling accurate reconstruction of full-length isoforms, including those spanning deletion
452 junctions. Although RACE-seq is less quantitative and has lower throughput, it provides higher
453 sensitivity for rare transcripts. Applying this framework to assess ASO-induced transcript

454 perturbations in organoids yielded fewer than 1,000 cells following treatment with either ASO-
455 Aplus (827 cells) or control ASO-NC (668 cells) (**Supplementary Table 2**). The limited recovery
456 likely reflects ASO-associated toxicity (**Extended Fig. 6a,b**) and reduced cell viability in day-222
457 organoids[62,63]. Long-read Capture-seq profiling of these samples provided high-resolution
458 transcriptome-wide splicing information; however, sequencing depth was insufficient to
459 comprehensively analyze splicing at sites SS4 and SS5 due to the limited number of recovered
460 cells. In this context, 5′ RACE-seq complemented Capture-seq by enabling detection of mutant
461 isoforms derived from the deletion allele when expression levels were low.

462 Some limitations should be noted. Both Capture-seq and RACE-seq remain constrained
463 by RNA integrity and read length, particularly in postmortem tissue. In addition, scRNA-seq
464 requires tissue dissociation, which disrupts cell–cell interactions and introduces dissociation bias,
465 limiting the ability to assess how *NRXN1* isoform perturbations reshape local cellular networks in
466 situ. Future integration with spatial transcriptomics could help preserve tissue architecture and
467 resolve cell–cell interactions. Another limitation of this study is the small number of patient-derived
468 samples. Specifically, we analyzed two organoids' lines carrying 3′-*NRXN1* deletions, along with
469 one ASD cerebellum sample harboring an *NRXN1* deletion and one control. This limited sample
470 size reflects both the rarity and non-recurrent nature of *NRXN1* exonic deletions in the currently
471 available biobank[3,64]. However, building on this study, we are in collaboration with a broad
472 research network of NRXN1 deletion and will expand the research to additional patient-derived
473 samples in future studies.

474 With the promise of ASO based gene therapy targeting RNA splicing, resolving transcript
475 diversity at cell-type resolution is essential for understanding the delivery and knockdown
476 efficiency. Our targeted long-read sequencing approach enables high-resolution characterization
477 of isoform usage and splicing shifts across distinct cell populations following ASO treatment,
478 providing a cell-type–specific readout of isoform knockdown efficiency. Overall, this study
479 demonstrates that targeted long-read sequencing offers a framework for comprehensive
480 characterization of low-abundance disease-associated transcript isoforms with cell type
481 specificity, with broad application to study natural isoform variations and the evaluation and
482 optimization of ASO-based interventions targeting pathogenic splicing events.

483

484

485 # FIGURE CAPTION

486 **Figure1. A targeting strategy reveals cell-type catalog of *NRXN1* isoforms.**

487 (a) *Upper panel* Bar graph showing the percentage of *NRXN1* reads detected by long-read
488 Capture-seq (orange) and non-targeted iso-seq (blue) across major brain cell classes. GABA,
489 GABAergic neurons; Glu, glutamatergic neurons; Astro, astrocytes; Micro, microglia; Oligo,
490 oligodendrocytes; OPC, oligodendrocyte progenitor cells. *Lower panel:* Fold change of *NRXN1*-
491 mapped reads obtained by long-read Capture-seq relative to the non-targeted single-cell Iso-
492 seq.
493 (b) Schematic illustrating the comprehensive characterization of cell-type-specific *NRXN1*
494 isoforms using the targeting strategy. Full-length single-cell/nuclei cDNA is divided into two
495 parts: one processed for a short-read library using Tn5 transposase and sequenced to identify
496 cell types; the other subjected to probe-based long-read Capture-seq and RACE-seq to detect
497 *NRXN1* isoforms with matched barcodes and UMIs (see Methods).
498 (c) *NRXN1* isoforms identified by single-cell long-read Capture-seq across samples. Each row
499 represents a unique isoform, categorized as α, α-mutant, β, γ, other known, or novel. Ensembl-
500 annotated isoforms are labeled with 'ENST' IDs. The heatmap shows presence (blue) or
501 absence (white) across adult prefrontal cortex, fetal neocortex, and human cortical organoids.
502 (d) PCA biplot of NRXN1 splicing profiles in GABAergic and glutamatergic neurons across
503 samples. Principal component analysis of mean inclusion fractions for exons at 6 splicing sites
504 (SS1-6). Arrows indicate SS event loadings with arrow direction showing which sample groups
505 have higher inclusion of corresponding events. The arrow length reflects the magnitude of
506 contribution to variance. A schematic of *NRXN1* gene structure is shown, with splice sites (SS1–
507 SS6) and alternatively spliced exons at each site highlighted in blue.
508

509 **Figure 2. *NRXN1* expression repertoires exhibit distinct splicing patterns across cell**
510 **types in human brains.**

511 **(a)** Workflow overview of long-read Capture-seq applied to single-nucleus cDNA from adult
512 PFC.
513 **(b)** UMAP visualization of putative cell types in the adult PFC. Colored clusters represent
514 neuronal and glial subtypes.
515 **(c)** Normalized *NRXN1* splicing events at six splicing sites (SS1–SS6) in GABAergic
516 interneurons (top), glutamatergic excitatory neurons (middle), and glial lineages (bottom). SS1–
517 3 represents exon 3 inclusion/ exclusion at splicing site, similar for SS1-4, SS2-7, *etc.* Each bar
518 represents a cell class. Within GABAergic interneurons, *PROX1*$^{+}$-INs are colored in green,
519 *LHX6*$^{+}$-INs in red, and *LAMP5*$^{+}$*LHX6*$^{+-}$INs in orange. Exon inclusion ("splice-in") is shown
520 upward and exclusion ("splice-out") downward. Data represent mean ± SEM. A schematic of
521 *NRXN1* gene structure is shown, with splice sites (SS1–SS6) and alternatively spliced exons at
522 each site highlighted in blue.
523 **(d)** PCA plot based on *NRXN1* splicing patterns across splice sites SS1–SS6, showing that
524 *PROX1*$^{+}$-INs, *LHX6*$^{+}$-INs, and PCs form distinct, separately clustered classes. Colors

525 correspond to cell types as in (c): *PROX1*$^{+}$- INs (green), *LHX6*$^{+}$-INs (red), *LAMP5*$^{+}$ *LHX6*$^{+}$-
526 GABAergic neurons (orange), glutamatergic neurons (blue), and glial lineages (gray).
527 (e) The difference in mean exon inclusion fraction between GABA and Glu neuronal cell types
528 (Δ = mean − mean) at 6 splicing sites. Positive values indicate higher inclusion in GABA
529 neurons; negative values indicate higher inclusion in Glu neurons. Significance labels denote
530 BH-adjusted *p*-values from Welch's t-tests (** $p < 0.01$; * $p < 0.05$; ns, not significant).

531 **Figure 3. *NRXN1* splicing profiles remain consistent across cells sharing a neurogenic**
532 **origin during neural maturation.**

533 (a)UMAP visualization of putative cell types in the neocortex from two fetal brains. *Left:* merged
534 UMAP of combined datasets; *Right:* separate UMAPs showing neocortex samples from 23 gw
535 and 33 gw. Colored clusters represent neuronal and glial subtypes in the fetal neocortex.
536 Abbreviations: gIPC, glutamatergic intermediate progenitor cells; RG/AC, radial glia/astrocyte
537 lineage; Ex, excitatory neurons; IN, inhibitory neurons; BVC, blood vessel cells; MG, microglia.
538 (b) The proportions of each cell class in 23 gw and 33 gw neocortex samples. Colored blocks
539 indicate neuronal and glial subtypes.
540 (c) Heatmap of marker genes expression used for cell-type annotation. Each row represents a
541 marker gene and each column a cell class; darker red indicates higher expression. Colored
542 blocks indicate neuronal and glial subtypes in fetal neocortex.
543 (d) Normalized *NRXN1* splicing events at SS1–SS6 in *PROX1*$^{+}$-INs (green), *LHX6*$^{+}$-INs (red),
544 glutamatergic excitatory neurons (blue), and glial lineages (gray). A schematic of *NRXN1* gene
545 structure is shown, with splice sites (SS1–SS6) and alternatively spliced exons at each site
546 highlighted in blue. Exon inclusion ("splice-in") is shown upward and exclusion ("splice-out")
547 downward. Data represent mean ± SEM.
548 (e) Pearson's correlation of *NRXN1* exon inclusion levels across splicing sites (SS1–SS6)
549 between adult PFC and prenatal neocortex in *LHX6*$^{+}$-INs (left), *PROX1*$^{+}$-INs(middle), and PC
550 neurons (right).
551

552 **Figure 4. *NRXN1*$^{+/-}$ human cortical organoids (hCOs) splicing profiles recapitulate**
553 **developmental and mature features and identify cell types expressing the mutant**
554 **isoforms.**

555 (a) *Left:* UMAP of putative cell types in hCOs, with colored clusters representing neuronal and
556 glial subtypes. *Right:* Proportions of each cell class in organoids derived from control line 690 or
557 3′-del lines (581 and 641). Abbreviations: gIPC, glutamatergic intermediate progenitor cells;
558 nIPC, neuronal intermediate progenitor cells; TAC, transient amplifying cells; RG/AC, radial
559 glia/astrocyte lineage; Ex, excitatory neurons; IN, inhibitory neurons; BVC, blood vessel cells.
560 (b) Heatmap of marker gene expression used for cell-type annotation. Each row represents a
561 marker gene and each column a cell type; darker red indicates higher expression.
562 (c) Bar graph showing enrichment of specific cell types in 3′-del organoids compared with
563 control lines.
564 (d) Normalized *NRXN1* splicing events at SS1–SS6 in all cell classes from control hCOs (upper)
565 and two 3′-del hCOs (lower). Each splicing graph is accompanied by a schematic of *NRXN1*

566 gene structure with red shading indicating 3′-del–associated regions; alternatively spliced
567 exons at each splice site are highlighted in blue. Exon inclusion is shown upward ("splice-in"),
568 exclusion downward ("splice-out"). Data represent mean ± SEM.
569 (e) Pearson's correlation of *NRXN1* exon inclusion levels across splicing sites (SS1–SS6)
570 between 3′-del and control hCOs.
571 (f) *Left:* Schematic of *NRXN1α* isoform structures identified by long-read RACE-seq, along with
572 a schematic of *NRXN1* gene structure. Red shading indicates regions associated with the 3′
573 deletion, and alternatively spliced exons at each splice site are highlighted in blue. Each row
574 represents a unique *NRXN1α* isoform, with blue exons indicating inclusion and blanks indicating
575 exclusion. *Right:* Presence or absence of each *NRXN1α* isoform across 3′-del and control hCOs
576 (green = present; blank = absent).
577 (g) The composition of *NRXN1* isoforms identified by long-read RACE-seq within each cell type
578 across 3′-del and the control hCOs.
579 (h) Exon inclusion levels at SS1–SS6 in GABAergic INs (top), glutamatergic excitatory neurons
580 (middle), and RG/AC (bottom) across hCOs (blue), fetal neocortex (orange), and adult PFC
581 (green). Statistical comparisons were performed using one-way ANOVA (*, $P < 0.05$; **, $P <$
582 0.01; ***, $P < 0.001$).Data represent mean ± SEM.

583

584 **Figure 5. A patient-specific *exonic* deletion drives cell-type–specific enrichment of**
585 **mutant *NRXN1* isoforms in the ASD cerebellum.**

586 (a) *Left:* UMAP of putative cell types in the cerebellum, with colored clusters representing
587 neuronal and non-neuronal subtypes. *Right:* Cell proportion of each cell class in the cerebellum
588 of ASD patient (*NRXN1*-del) and the control.
589 (b) Schematic of *NRXN1* isoform structures identified by long-read capture-seq, with each row
590 representing a unique *NRXN1* isoform. The $NRXN1^{+/-}$ specific mutant isoforms are highlighted in
591 red.
592 (c) Expression level of *NRXN1* isoforms (expression level as TPM) from cerebellum of control or
593 *NRXN1*-del. The red box highlights mutant isoforms specific to the deletion-carrying allele.
594 (d) The proportion of cells in each cell class expressing any *NRXN1* isoforms, wild-type
595 isoforms(*NRXN1*-WT) and mutant isoforms (*NRXN1*-MT).
596 (e) Normalized *NRXN1* splicing events at SS1–SS6 for Granule and MLI1/2 cells from $NRXN1^{+/-}$
597 (*NRXN1*-del) and control (Br1446) cerebellum. Schematic splice graph of *NRXN1* depicting
598 splice sites (SS1–SS6), with red shading marking regions impacted by the exonic deletion
599 allele. Alternatively spliced exons at each splice site are highlighted in blue. Exon inclusion is
600 shown upward ("inclusion") and exclusion downward ("exclusion"). Data represent mean ± SEM.
601 (f) Aggregate enrichment of GO terms within each biological theme across cell types by
602 down-regulated (blue) and up-regulated (red) DEGs, excluding themes implicated by only
603 one term and nonsignificant cell types.
604 (g) Overrepresentation of synaptic compartment genes [SynGO database[65]] within cell type–
605 specific DEGs. $^{*}P < 0.05$, $^{**}P < 0.01$, $^{***}P < 0.001$, Hypergeometric test, FDR < 0.05.

606

Figure 6. Evaluation framework for cell-type–resolved ASO inhibition of GOF *NRXN1* isoforms in cortical organoids.

(a) *Left:* UMAP of putative cell types in ASO-treated hCOs derived from line 641, with colored clusters representing neuronal and glial subtypes. *Right:* Proportions of each cell class in line 641 treated with ASO-NT or ASO-Aplus.

(b) Splicegraphs displaying the splicing of the MT exon 20→24 cluster in 641 hCOs treated with ASO-Aplus (upper) or ASO-NT(lower), compared via a Dirichlet-multinomial generalized linear model.

(c) Cell-type–specific mapping of NRXN1 reads (containing exons 20–24) following ASO-NT or ASO-Aplus treatment. Color coding of cell types corresponds to the scheme used in the UMAP (Fig. 6a).

(d) Percentage of wildtype or mutant *NRXN1* isoforms detected by long-read RACE-seq across cell types in 641 hCOs with ASO treatment. A significant enrichment of the wildtype isoform in nIPCs is observed in the 641-Aplus condition (OR = 0.015, $p = 1.53 \times 10^{-7}$, BH-adjusted $p = 6.13 \times 10^{-7}$, Fisher's Exact test).

(e) Normalized *NRXN1* splicing events at SS1–SS6 for neuronal (EXs and INs) and non-neuronal (RG/AC, nIPC) cells in 641 hCOs treated by ASO-Aplus treated (left) or ASO-NT (right). Exon inclusion is shown upward ("splice-in") and exclusion downward ("splice-out"). Data represent mean ± SEM.

METHODS

Data Availability

Raw long-read sequencing data have been deposited in the Sequence Read Archive under accession number PRJNA1447486. Processed and raw single-cell RNA sequencing (scRNA-seq) data, including gene–cell count matrices and associated metadata, have been deposited in the Gene Expression Omnibus under accession number GSE327718 (to be updated upon release).

Acquisition and processing of human post-mortem samples

The MSSM cohort single nuclei cDNA. The sequencing data and full-length single-nucleus cDNA libraries of 61 individuals from the Mount Sinai School of Medicine cohort were generated from the previous publication[27]. The leftover barcoded full length single-nucleus cDNA was used as input for the current study. To obtain 1-1.5 µg of cDNA for the hybridization step, 5-10 ng of the surplus barcoded 10x cDNA was amplified in two 50 µl reactions, which consist of 25 µL 2X PrimeSTAR GXL premix (Takara, Cat# R051A), 1 µL partial read 1 primer (10 µM, 5'-CTACACGACGCTCTTCCGATCT-3'), 1 µL partial TSO primer (10 µM, 5'-AAGCAGTGGTATCAACGCAGAG-3'). The amplification program is set as follows: 98 °C for 30 seconds, 8 cycles of 98 °C for 10 seconds, 65 °C for 15 seconds and 68 °C for 8 minutes, 1 cycle of 68 °C for 10 minutes. The concentration of PCR products was quantified by Qubit, and additional cycles were added if the yield was lower than 500 ng per reaction. The PCR products were cleaned up with 0.6× AMPure XP beads.

***NRXN1*$^{+/-}$ cerebellum of human post-mortem brain.**

647 Postmortem human cerebellum of the ASD case with a heterozygous *NRXN1*$^{+/-}$ mutation were
648 collected and consented through the Department of Pathology at Western Michigan University
649 Homer Stryker MD School of Medicine under WCG IRB protocol #20111080 and the other
650 samples were consented through the National Institute of Mental Health Intramural Research
651 Program under NIH protocol #90-M-0142, and was acquired by LIBD via material transfer
652 agreement.

653 **Fetal brain.** Two human gestational cortical tissue samples (24 gw and 33 gw) were obtained
654 from previous study [36] in accordance with the policies and regulations at the Icahn School of
655 Medicine at Mount Sinai and its Institutional Review Board.

656 **Single cell/nucleus full-length barcode cDNA**. 60mg of the frozen post-mortem tissues were
657 submitted to Yale Center for Genome Analysis for single nuclei isolation. Briefly, single nuclei
658 were automatically extracted from the frozen tissue using the Singulator system, which includes
659 washing nuclei suspension in buffer supplemented with sucrose, and nuclei FACS sorting. The
660 isolated nuclei were then processed using the 10x Genomics 5'GEX V2 to create single nuclei
661 cDNA and matched short-read RNA-seq libraries per manufacturer's instructions.

662 **Patient-derived organoids**

663 Human induced pluripotent stem cell (hiPSC) lines used were validated using methods as
664 previously described. Genome-wide SNP genotyping was performed using Illumina genome-wide
665 GSAMD-24v2-0 SNP microarray at the Children's Hospital of Philadelphia. Cultures were tested
666 for Mycoplasma contamination and maintained Mycoplasma-free. A total of 3 hiPS cell lines
667 derived from fibroblasts collected from 1 healthy subject (690) and two 3'-del lines from two
668 patients (581 & 641) were used for experiments. Approval for this study was obtained from the
669 Stanford IRB panel, and informed consent was obtained from all subjects.

670 **Stem cell maintenance**. Human iPSCs were obtained as previously described in Flaherty et
671 al., 2019. Under sterile conditions, 6-well plates (Corning 3516) were coated with 60 ug/mL
672 Geltrex matrix (Thermo Fisher Scientific A1413302) diluted in Dulbecco's Modified Eagle
673 Medium (DMEM, Gibco 11965-092) per well and incubated for at least 30 min at 37 °C. All
674 hiPSC lines were seeded on coated plates and maintained in StemFlex (StemFlexTM Basal
675 Medium (Gibco A3349301) supplemented with StemFlexTM Supplement (Gibco A3349201)) at
676 37 °C. After 4 days, hiPSC lines were passaged by removing the media washing cells with PBS.
677 Then cells were incubated in 0.5 μM EDTA in PBS (Invitrogen AM9261) for 4 min at 37 °C. After
678 removing EDTA, colonies were broken into smaller pieces by triturating using a p1000 pipette
679 and StemFlex. It is worth noting that very small colonies have a very low survival chance and
680 should be supplemented with 50nM chroman (CHR; MedChemExpress, Cat. No. HY-15392).
681 After dissociation, colonies were distributed in new coated plates containing StemFlex in a ratio
682 of 1:6 (250K cell per well of a 6 well plate). A complete media change was performed the
683 following day. Complete media changes were performed as needed or every other day.

684 **Cortical organoid generation**. Cultures of hiPSC were dissociated at 70% confluency and
685 checked for signs of differentiation. Mature undifferentiated cells were washed with PBS,
686 followed by incubation with Accutase (STEMCELL™ Technologies, Cat. No. 07920 and CHR for
687 10-20 min to achieve complete detachment. Cells were gently triturated to achieve a single-cell
688 suspension. The resulting cell suspension was transferred into DMEM (Gibco, Cat. No.
689 11960044) and centrifuged at 500 × g for 4 min. Cells were resuspended in StemFlex™
690 medium (Thermo Fisher Scientific) supplemented with CHR and diluted at a density of 1.5 ×

691 10^6 cells/mL. AggreWell™ plates (STEMCELL Technologies) were prepared with anti-
692 adherent solution according to the manufacturer's instructions. A volume of 2 mL of the hiPSC
693 suspension was seeded per well to promote spheroid formation overnight (defined as day 0).
694 Neural induction was subsequently performed following the human forebrain spheroid protocol
695 described by Sloan *et al*[66]. In brief, medium was replaced daily until day 15, every other day
696 from days 15–42, and every 4 days from day 43 onward. On day 1, embryoid bodies were
697 dislodged and transferred to ultra-low adhesion 10 cm dishes containing Neuronal Induction
698 Media (StemFlex™ medium without StemFlex™ supplement), SMAD inhibitors SB431542 (10
699 μM ; R&D Systems/Tocris Bioscience,1614), LDN193189 (100 nM; STEMCELL Technologies,
700 1614), XAV (100nM; STEMCELL Technologies,72672). Plates were placed on an orbital shaker
701 at 53 rpm and maintained at the same speed until day 6. From days 6–25, Neuronal
702 Differentiation Media (Neurobasal-A (Thermo Fisher Scientific), 1x Antibiotic-Antimycotic
703 (Gibco,15240062), 1x GlutaMAX™(Gibco, Cat. No. 5050061), and 1x B-27 supplement minus
704 vitamin A (Gibco, Cat. No. 2587010) was used supplemented with recombinant human
705 FGF2/bFGF (20 ng/mL; R&D Systems, Cat. No. 233-FB-01M) and recombinant human EGF (20
706 ng/mL; R&D Systems, Cat. No. 236-EG). Between days 25–42, Neuronal Differentiation Media
707 was supplemented with brain-derived neurotrophic factor (BDNF; 100 nM; R&D Systems, Cat
708 No.248-BD-025) and neurotrophin-3 (NT-3; 100 nM; PeproTech, Cat No.450-03). From day 42
709 onwards, organoids were maintained in Neuronal Differentiation Media.

710 **Cryoprotection and immunocytochemistry**. Organoids were washed with PBS and fixed in 4%
711 paraformaldehyde (PFA)/phosphate buffered saline (PBS) for 3 to 4 hours overnight at 4°C.
712 Organoids were then washed in PBS and transferred to 25% sucrose/H_2O for 48 hours. Organoids
713 were embedded in gelatin/sucrose embedding solution by dissolving 7.5 g gelatin in 100 ml 10%
714 sucrose solution at 37°C to obtain a 7.5% gelatin/10%sucrose embedding solution. For
715 immunofluorescence staining, 14-16 μm-thick sections were washed with PBS and blocked in
716 10% donkey serum, and 0.1% Triton-X in PBS for 1 h at room temperature followed by primary
717 (overnight, 4 °C) and secondary antibody (1 h at room temperature, Jackson ImmunoResearch or
718 ThermoFisher Scientific) incubation. Slides were then mounted (VECTASHIELD, Vector Labs)
719 and imaged on a Zeiss microscope with an apotome module equipped with ZEN 3.3 (ZEN pro)
720 software.

721 Primary antibody list:. Primary Antibody list: *BCL11B/CTIP2* (rat, 1:500, Abcam), *FOXG1* (rabbit,
722 1:200, Abcam), *GAD1/GAD67* (mouse, 1:1000, Millipore), *HuC/D* (mouse, 1:500, Invitrogen),
723 *KI67* (rabbit, 1:500, Vector Labs), *PAX6* (mouse, 1:200, BD Bioscience), *SOX1* (goat, 1:20,
724 R&D Systems), *TBR1* (rabbit, 1:1000, Abcam).

725

726 **Antisense oligonucleotide treatment.** A single HPLC-purified antisense oligonucleotide (ASO)
727 targeting the mutant exon 20/24 splice junction was designed and synthesized by IDT. The ASO
728 contains a phosphorothioate-modified backbone with incorporated locked nucleic acid (LNA)
729 nucleotides (Affinity Plus, Aplus). A non-targeting ASO (ASO-NT) was used as a matched
730 control in all experiments. The sequence of ASO-Aplus as
731 +G*+G*+T*T*G*G*C*T*G*C*A*G*G*+G*+T*+A; and the sequence of ASO-NT as
732 A*A*C*A*C*G*T*C*T*A*T*A*C*G*C. To optimize delivery conditions and dosage, human
733 cortical organoids (hCOs) derived from line 641 (3′-*NRXN1*$^{+}$/$^{-}$) at day 222 were treated with 1
734 μM or 10 μM ASO-Aplus or ASO-NT, delivered either via Lipofectamine RNAiMAX[67] or
735 gymnosis, and incubated for 96 h prior to qPCR validation or single-cell and RNA collection.

736 Expression levels of mutant and wild-type *NRXN1* transcripts were quantified by qPCR to
737 assess ASO knockdown efficiency.

738 **Single-cell dissociation and RNA-seq library preparation.** Organoids with optimal morphology
739 from each line were selected in days 25, 60, and 120. Five organoids from each line were pooled
740 at each time point and transferred to a 5 cm plate dish and washed with PBS. Organoids were
741 chopped into small pieces using a sharp sterile blade. 300 ul of Accumacs was added on top of
742 the pieces without scattering them. Pieces were collected by a cut tip and were transferred into a
743 1.5 ml tube. The tubes were incubated at 37°C and 800 g rotation on a thermal shaker for 20 min.
744 After 20 min, cell suspension was very gently pipetted up to 5 times with a p 1000 tip, to facilitate
745 the cell dissociation. 500 ul fresh Accumacs was added into the suspension and incubated again
746 for 20 min. Cell suspension was pipetted up to 5 times more and passed through a filter in a 15
747 ml sterile tube containing 1 ml of HEPES buffer. The filter was washed with 1 ml of HEPES buffer.
748 The single cell suspension in a 15 ml tube was centrifuged at 300 g for 4 min to collect cells in a
749 pellet. After removing the supernatant, the pellet was resuspended in 200 ul HEPES buffer and
750 cells were counted using a hemocytometer. The suspension was diluted to reach 1200 cell per
751 ml and was submitted to Yale Genomics Core facility for cDNA library prep using 10x 5' NEXT
752 GEM V2 according to the manufacturer's instructions.

753 **NGS sequencing of single cell/ nucleus cDNA**

754 The prepared 10X Genomics single cell/nucleus libraries were submitted to Yale Center for
755 Genome Analysis and sequenced on an Illumina NovaSeq sequencer with 150-bp paired-end
756 sequencing on an S4 flow cell. For each sample, ~10,000 cells were sequenced at a minimum
757 depth of 50,000 reads per cell.

758 **Probe-panel design**

759 IDT Lockdown probes (Integrated DNA Technologies) are 120-nt long oligos that are
760 biotinylated at their 5' ends and were designed using the xGen Panel Design Tool
761 (https://www.idtdna.com/pages/tools/xgen-hyb-panel-design-tool) to ensure robust coverage of
762 the targeted regions. Briefly, a customized *fasta* file containing all Ensembl[26]-annotated exons
763 (across all isoforms) of target genes, including UTRs was uploaded as input file. The probe
764 sequence list was generated at the 1x probe tilling density using "Homo sapiens (Human) NCBI
765 GRCh37.p13 (hg19)" as the reference (Supplementary table 1).

766 The probe panel was further synthesized employing TEQUILA-seq[21]. First, the probe panel pool
767 of 150-nt long oligos, each comprising a 3' end 30-nt universal primer binding sequence (5'-
768 CGAAGAGCCCTATAGTGAGTCGTATTAGAA-3') followed by a 120-nucleotide target-specific
769 probe, was synthesized with Twist Bioscience (Supplementary table 1). Then the oligo pools
770 were amplified and biotin-labeled using nickase-induced linear strand displacement
771 amplification as described previously. Finally, synthesized probes were purified with 1.8×
772 volumes of AMPure XP beads and quantified by NanoDrop 2000 Spectrophotometer.

773 **Long-read Capture-seq on single cell/ nucleus cDNA**

774 All hybridization and capture steps were performed following the IDT "Hybridization capture of
775 DNA libraries using xGen Lockdown probes and reagents" protocol. Briefly, 1-1.5 µg of
776 amplified 10x cDNA together with 1 µL of each blocking oligos (1 mM, **Supplementary Table1**)
777 were dried using a speed vac (Thermo, Cat# SPD140P1). Next, the dried sample were re-
778 hydrated with 8.5 µL of 2× Hybridization Buffer, 2.7 µl Hybridization Buffer Enhancer (xGen IDT

779 1080577), and 3.8 µL nuclease-free water, followed by denaturation at 95 °C for 10 min. The
780 denatured mixture was then incubated with 200 ng of TEQUILA probes at 65 °C for 16 h. Next,
781 the capture step was performed by adding 100 µL of washed M-270 streptavidin beads
782 (Invitrogen, #65306) to the mixture, followed by incubation at 65 °C for 45 minutes with vortexing
783 every 10 minutes to ensure thorough mixing. After capture, the mixture was then immediately
784 washed with high-temperature and room temperature buffers and resuspended in 40 µL
785 nuclease-free water.

786 The streptavidin bead-captured cDNA was amplified using PrimeSTAR GXL premix (Takara,
787 Cat# R051A) and 10x cDNA amplification primers by incubating at 95 °C for 3 min, followed by
788 12 cycles of (98 °C for 20 s, 65 °C for 15 s, 68 °C for 8 min), with a final extension at 68 °C for
789 8 min. Post-capture PCR products were purified using 0.7× volumes of AMPure XP beads, and
790 quantified by the Qubit dsDNA High Sensitivity assay and size checked by Agilent TapeStation.

791 **Gene-targeted single cell/ nucleus RACE-PCR**

792 To sequence the *NRXN1α* isoforms and 10x single cell barcode from one long-read, the
793 modified RACE-PCR was employed to amplify the target from the 10x Genomics 3'GEX or
794 5'GEX cDNA. 5'RACE was used for cDNA generated by 10x 5'GEX kit, while 3'RACE was used
795 for cDNA generated by 10x 3'GEX kit.

796 **PCR primer design**. As the expression level of *NRXN1α* is relatively low in adult brains, nested
797 PCR would be needed to achieve enough molecules. The gene-specific primers (GSPs) should
798 meet the criteria: 23-28 nt long to ensure specific annealing, with 50%-70% GC, a T_m 65°C
799 (best to have a T_m >70°C) and be specific to the target gene (**Supplementary Table 1**).
800 Universal primers: The universal primer for first -round PCR should be the partial read1
801 sequence from 10x cDNA. To increase sensitivity for the second-round PCR, a sequence of
802 "AATGATACGGCGACCACCGAGATCT" was added to the 5' of the read1 (**Supplementary**
803 **Table 1**), forming the second-round universal PCR primer (UP2) (**Supplementary Table 1**).

804 **Protocol**. The input of 1-50 ng of 10x 5'GEX or 3'GEX cDNA was used for the RACE-PCR. The
805 first round of RACE-PCR is carried out with 1 µL partial Read1 primer (10 µM) and 4 µL *NRXN1*
806 -specific primer 1 (10 µM) in a 50 µl-reaction, which consists of additional 25 µL 2X PrimeSTAR
807 GXL premix (Takara, Cat# R051A), 1-50 ng of full-length single cell cDNA by 10x 5'GEX or
808 3'GEX kit. Choose the PCR program based on the GSP T_m . Program 1: when GSP T_m >70°C,
809 run 5 cycles of 94°C for 30s, 72°C for 8min; 5 cycles of 94°C for 30s, 70°C for 30s and 72°C for
810 8min; 15-20 cycles of 94°C for 30s, 68°C for 30s and 72°C for 8min. Program 2: when T_m = 60-
811 70°C, run 15-20 cycles of 94°C for 30s, 68°C for 30s and 72°C for 8min. The concentration of
812 PCR products was quantified by Qubit, and additional cycles can be added if the concentration
813 of PCR product is lower than 10 ng/µL. After the PCR, 3 µL of products were analyzed with 1%
814 agarose/ GelRed gel (biotium, cat# 41002), while the rest products were purified using 0.7×
815 volumes of AMPure XP beads and eluted with 30 µL nuclease-free water. If the primary PCR
816 fails to show the distinct band(s) of interest or produces a smear, a second-round of RACE-PCR
817 should be performed.

818 The second-round of RACE-PCR is performed with 2.5 µL of UP2 (10 µM) and 2.5 µL *NRXN1*-
819 specific primer 2 (10 µM) in a 50 µl-reaction together with 25 µL 2X PrimeSTAR GXL premix
820 and 10 µL of the purified first-round RACE-PCR products. The PCR program follows the
821 program 2 and runs for 10-15 cycles based the final concentration of PCR products. After the
822 PCR, 3 µL of products were analyzed with 1% agarose/ GelRed gel for size check, which is
823 followed by the purification using 0.7× volumes of AMPure XP beads.

824 **Library preparation for Oxford Nanopore sequencing**

825 Oxford Nanopore SQK-NBD114.24 was used for library preparation. Amplified cDNA from post-
826 capture of RACE-PCR, approximately 200 ng of PCR products from each sample were used for
827 library preparation according to the ONT SQK-NBD114.24 protocol. Briefly, cDNA products
828 were end-repaired and dA-tailed with NEBNext Ultra II End Repair/dA-Tailing Module by
829 incubating at 20 °C for 30 min and 65 °C for 30 min. The cDNA was then purified with 1× volume
830 of AMPure XP beads and eluted in 10 µl of nuclease-free water. Native barcode ligation was
831 then performed using 10 µl of end-prepped DNA, 2.5 µl of native barcodes, and 12.5 µl of
832 Blunt/TA Ligase Master Mix (NEB, #M0367) by incubating at room temperature for 30 min. After
833 the ligation step, 2.5 µl of EDTA was added to each tube to inactivate the ligase. Barcoded
834 cDNA samples were then pooled and purified using 0.4× volume of AMPure XP beads and
835 eluted in 31 µl of nuclease-free water. Next, ligation of Native Adapter was performed with 30 µl
836 of pooled barcoded samples, 5 µl of native adapter, 10 µl of 5× NEBNext Quick ligation reaction
837 buffer, and 5 µl of NEBNext Quick T4 DNA ligase at room temperature for 30 min, followed by
838 the bead's purification using 0.45× volume of AMPure XP beads and twice wash with short
839 fragment buffer. The libraries were quantified with Qubit, and 50 fmol of final library was
840 sequenced with a R10.4.1 MinION or PromethION flow cell for 72 hours.

841 **Single-cell RNA-seq processing and analysis**

842 Raw 10x Genomics single-cell RNA-seq data were processed using Cell Ranger (v7.2.0) with the
843 GRCh38 reference genome to generate gene-cell UMI count matrices. Downstream analyses
844 were performed in Seurat (v5.0.3)[68] under R (v4.4.0). Cells with fewer than 200 detected genes,
845 more than 6,000 detected genes, or mitochondrial transcript fractions exceeding 20% were
846 excluded. Potential doublets were identified and removed using DoubletFinder[69]. See the
847 sequencing summary in **the Supplementary Table 2**.

848 Post-quality control, gene expression values were normalized by scaling each cell's total
849 expression to 10,000 counts and log-transforming the results. Data were then processed using
850 SCTransform[68], which performs regularized negative binomial regression to normalize and correct
851 for sequencing depth and mitochondrial content. Highly variable genes were selected for PCA,
852 and dimensionality reduction was performed using UMAP.

853 Clustering was conducted using a shared nearest neighbor (SNN) graph and the Louvain
854 algorithm to identify transcriptionally distinct populations. Cell type annotation was guided by
855 canonical marker gene expression and cross-referenced with public human brain (or tissue-
856 specific) single-cell catalogs. Differential expression analyses between groups or clusters were
857 performed using the Wilcoxon rank-sum test with Benjamini-Hochberg correction for multiple
858 testing (FDR < 0.05).

859 Following dimensionality reduction and clustering, known marker genes were used to guide the
860 assignment of biological cell identities. Each cluster was annotated based on the expression of
861 established cell-type-specific markers reported in previous studies.

862 GO Biological Process (BP) enrichment analysis was performed for each cell type using
863 differentially expressed genes (DEGs) identified between ASD and control samples. Up- and
864 downregulated DEGs were analyzed separately. Enrichment was tested
865 using clusterProfiler (v4.12.6) with a background of all genes tested in that cell type (18,903
866 genes). Significant GO terms were retained at FDR < 0.05 (Benjamini–Hochberg correction). For
867 each cell type and direction, up to the top 200 most significant terms were carried forward for

868 downstream clustering. To reduce redundancy among significant GO BP terms and identify broad
869 biological themes, semantic similarity clustering was performed using the rrvgo R package. For
870 each direction (up/down), a pairwise semantic similarity matrix was computed across all
871 significant GO terms pooled from all cell types. Terms were clustered into representative parent
872 terms using reduceSimMatrix with a similarity threshold of 0.7. Each GO term was scored as the
873 maximum $-\log_{10}$(FDR) observed across all cell types. The resulting clusters were summarised
874 into biological themes, and the top 20 themes ranked by the number of cell types with significant
875 signal are displayed. For each cell type × theme combination, the cell in the heatmap represents
876 the maximum $-\log_{10}$(FDR) across all member GO terms within that cluster. Enrichment of DEGs
877 within synaptic compartments was assessed using the SynGO database (v1.3). Three cellular
878 component categories were tested: Synapse, Presynapse, and Postsynapse. For each cell type
879 and direction (up/down), a one-sided hypergeometric test. Multiple testing correction was applied
880 using the Benjamini–Hochberg method across all cell type × compartment combinations within
881 each direction. Enrichments with FDR < 0.05 were considered significant.

882

883 **Long-read isoform sequencing analysis**

884 Full-length transcript isoforms were characterized using long-read RNA sequencing (Oxford
885 Nanopore or PacBio). Raw reads were basecalled using dorado (v0.4.1). Reads were quality-
886 filtered to retain those with a minimum mean Phred quality score of Q10 and minimum read length
887 of 200 bp, and adapter sequences were trimmed prior to alignment. Processed reads were
888 aligned to the human reference genome (GRCh38) using minimap2 (v2.28) with cDNA splice-
889 aware parameters (-ax splice --secondary=no -C5). Alignments were coordinate-sorted and
890 indexed using SAMtools (v1.21), and only primary alignments with a minimum mapping quality of
891 MAPQ $\geq$ 10 were retained for downstream analysis. Isoform reconstruction and quantification
892 were performed using IsoQuant (v3.2) with GENCODE v43 as reference annotation. IsoQuant[70]
893 clusters reads into high-confidence transcript models, classifying each as known, novel in catalog
894 (NIC), or novel not in catalog (NNC) based on splice junction composition. Only isoforms
895 supported by at least three full-length reads were retained.

896 Differential splicing analysis was performed using LeafCutter[71]. Briefly, splice junctions were
897 extracted from BAM files using RegTools, with a minimum anchor length of 8 bp and intron size
898 ranging from 50 to 500,000 bp. Junction files from all samples were combined and clustered into
899 intron groups using the LeafCutter clustering pipeline, requiring a minimum of 50 supporting
900 reads per cluster.

901

902 **Integration of long-read isoform data with short-read single-cell transcriptomes**

903 Integration between long-read and short-read data was performed at both the gene and isoform
904 levels. Cell barcode and UMI assignment from Nanopore reads was accomplished using BLAZE
905 (v1.4.0)[72], which accurately detects 10x cellular barcodes and unique molecular identifiers
906 (UMIs) directly from Nanopore cDNA reads. BLAZE localizes barcode sequences within read
907 adapter contexts, compares candidate sequences against the 10x whitelist, and assigns valid
908 barcodes with up to one mismatch tolerance to each read. This enabled unambiguous
909 association of long reads with individual cell identities and facilitated construction of a cell ×
910 isoform count matrix for isoform-level single-cell analysis.

NRXN1 Isoform Quantification using *miniQuant*

For the BA4 samples, *miniQuant*[73] was applied in hybrid mode, integrating both short-read and long-read RNA-seq generated in-house to improve isoform-level quantification. For the FC and hippocampus datasets[25,74], where only long-read RNA-seq data were available, *miniQuant* was applied in long-read-only mode to estimate isoform abundances.

In *miniQuant*, long-read cDNA sequencing provides high-confidence isoform structures and reduces ambiguity in assigning reads to specific isoforms, whereas short-read sequencing improves quantification accuracy for low-abundance transcripts by reducing sampling error. *miniQuant*'s gene-specific weighting model adaptively balances these complementary data sources based on isoform structural complexity (K-value), transcript abundance, and sequencing depth, producing optimized isoform abundance estimates. Isoform expression levels were reported as transcripts per million (TPM) to allow direct comparison across samples.

To ensure quantification reliability, we filtered out low-confidence isoforms following the criteria described in the original *miniQuant* framework, requiring both sufficient long-read support and a minimum expression threshold. Only isoforms with TPM ≥ 1 in at least one sample were retained for downstream analyses.

Data visualization and statistical analysis

All visualizations, including UMAPs, dot plots, violin plots, and bar plots, were generated in *R* or *Python* using the *ggplot2*, *matplotlib*, and *seaborn* libraries. For continuous variables, such as comparisons of AS event inclusion levels or isoform expression differences, we applied *Welch's t-test*, which does not assume equal variances between groups.

ACKNOWLEDGEMENTS

We thank Daniel Weinberger and the Lieber Institute for Brain Development at Johns Hopkins School of Medicine, for sharing post-mortem brain tissues. We thank Feng Wang and Yi Xing (Children's Hospital of Philadelphia) for technical assistance with TEQUILA-seq. This work is supported by the National Institute of Mental Health grants RO1 MH125579 (GF and KJB) and RO1 MH121074 (KJB and GF), and U01MH116442 (PR) and R01MH125246 (PR). Research reported in this publication was supported by the National Institute of General Medical Sciences of the National Institutes of Health under Award Number 1S10OD030363-01A1. N.A.L.H. was supported by the National Institute for Health and Care Research (NIHR) Oxford Health Biomedical Research Centre. This work was also supported in part through the computational resources and staff expertise provided by the Department of Scientific Computing at the Icahn School of Medicine at Mount Sinai.

AUTHOR CONTRIBUTIONS

LC, YF and GF designed the methods. LC and YF performed targeted long-read sequencing and conducted data analysis. SG generated cortical organoids, and JM performed ASO treatments. YZ assisted with bioinformatic analyses. MBF designed the ASO. JB, JF, and PR provided single-nuclei RNA sequencing data from adult post-mortem brains and contributed to data analysis. SIR and NT provided post-mortem fetal brain tissues. NH provided technical assistance with Capture-seq. GD, KGB, and RS assisted with long-read sequencing. BZ and SM provided technical assistance with single-nuclei cDNA preparation. EAM contributed to data

analysis and interpretation. LC, YF, SG, KJB and GF wrote the manuscript with input from all authors. KJB and GF supervised the research.

COMPETING INTERESTS

The authors declare no competing interests.

959 **REFERENCES**

960 1. Fagnani, M. *et al.* Functional coordination of alternative splicing in the mammalian central
961 nervous system. *Genome Biol.* **8**, R108 (2007).

962 2. Raj, B. & Blencowe, B. J. Alternative splicing in the mammalian nervous system: recent
963 insights into mechanisms and functional roles. *Neuron* **87**, 14–27 (2015).

964 3. Furlanis, E., Traunmüller, L., Fucile, G. & Scheiffele, P. Landscape of ribosome-engaged
965 transcript isoforms reveals extensive neuronal-cell-class-specific alternative splicing
966 programs. *Nat. Neurosci.* **22**, 1709–1717 (2019).

967 4. Lipscombe, D. & Soto, E. J. L. Alternative splicing of neuronal genes: new mechanisms
968 and new therapies. *Curr. Opin. Neurobiol.* **57**, 26–31 (2019).

969 5. Gomez, A. M., Traunmüller, L. & Scheiffele, P. Neurexins: molecular codes for shaping
970 neuronal synapses. *Nature Reviews Neuroscience* vol. 22 137–151 Preprint at
971 https://doi.org/10.1038/s41583-020-00415-7 (2021).

972 6. De Wit, J. & Ghosh, A. Specification of synaptic connectivity by cell surface interactions.
973 *Nat. Rev. Neurosci.* **17**, 4 (2016).

974 7. Südhof, T. C. Synaptic neurexin complexes: a molecular code for the logic of neural
975 circuits. *Cell* **171**, 745–769 (2017).

976 8. Harkin, L. F. *et al.* Neurexins 1-3 each have a distinct pattern of expression in the early
977 developing human cerebral cortex. *Cerebral Cortex* **27**, 216–232 (2017).

978 9. The role of neurexins and neuroligins in the formation, maturation, and function of
979 vertebrate synapses.

980 10. Schreiner, D. *et al.* Targeted Combinatorial Alternative Splicing Generates Brain Region-
981 Specific Repertoires of Neurexins. *Neuron* **84**, 386–398 (2014).

982 11. Treutlein, B., Gokce, O., Quake, S. R. & Südhof, T. C. Cartography of neurexin
983 alternative splicing mapped by single-molecule long-read mRNA sequencing. *Proc. Natl.*
984 *Acad. Sci. U. S. A.* **111**, (2014).

985 12. Flaherty, E. *et al.* Neuronal impact of patient-specific aberrant NRXN1α splicing. *Nat.*
986 *Genet.* **51**, 1679–1690 (2019).

987 13. Uemura, T. *et al.* Trans-synaptic interaction of GluRδ2 and Neurexin through Cbln1
988 mediates synapse formation in the cerebellum. *Cell* **141**, 1068–1079 (2010).

989 14. Siddiqui, T. J. *et al.* An LRRTM4-HSPG complex mediates excitatory synapse
990 development on dentate gyrus granule cells. *Neuron* **79**, 680–695 (2013).

991 15. Boucard, A. A., Chubykin, A. A., Comoletti, D., Taylor, P. & Südhof, T. C. A splice code
992 for trans-synaptic cell adhesion mediated by binding of neuroligin 1 to α-and β-neurexins.
993 *Neuron* **48**, 229–236 (2005).

994 16. Ko, J., Fuccillo, M. V, Malenka, R. C. & Südhof, T. C. LRRTM2 functions as a neurexin
995 ligand in promoting excitatory synapse formation. *Neuron* **64**, 791–798 (2009).

996 17. Fuccillo, M. V *et al.* Single-cell mRNA profiling reveals cell-type-specific expression of
997 neurexin isoforms. *Neuron* **87**, 326–340 (2015).

998 18. Freund, T. F. & Katona, I. Perisomatic inhibition. *Neuron* **56**, 33–42 (2007).

999 19. Fernando, M. B. *et al.* Phenotypic complexities of rare heterozygous neurexin-1 deletions.
1000 *Nature* 1–11 (2025).

1001 20. Lukacsovich, D. *et al.* Single-cell RNA-seq reveals developmental origins and ontogenetic
1002 stability of neurexin alternative splicing profiles. *Cell Rep.* **27**, 3752–3759 (2019).

1003 21. Wang, F. *et al.* TEQUILA-seq: a versatile and low-cost method for targeted long-read
1004 RNA sequencing. *Nat. Commun.* **14**, (2023).

1005 22. Ray, T. A. *et al.* Comprehensive identification of mRNA isoforms reveals the diversity of
1006 neural cell-surface molecules with roles in retinal development and disease. *Nat.*
1007 *Commun.* **11**, (2020).

1008 23. Ohara, O., Dorit, R. L. & Gilbert, W. One-sided polymerase chain reaction: the
1009 amplification of cDNA. *Proceedings of the National Academy of Sciences* **86**, 5673–5677
1010 (1989).

1011 24. Frohman, M. A., Dush, M. K. & Martin, G. R. Rapid production of full-length cDNAs from
1012 rare transcripts: amplification using a single gene-specific oligonucleotide primer.
1013 *Proceedings of the National Academy of Sciences* **85**, 8998–9002 (1988).

1014 25. Hardwick, S. A. *et al.* Single-nuclei isoform RNA sequencing unlocks barcoded exon
1015 connectivity in frozen brain tissue. *Nat. Biotechnol.* **40**, 1082–1092 (2022).

1016 26. Dyer, S. C. *et al.* Ensembl 2025. *Nucleic Acids Res.* **53**, D948–D957 (2025).

1017 27. Ruzicka, W. B. *et al.* Single-cell multi-cohort dissection of the schizophrenia
1018 transcriptome. *Science (1979).* **384**, eadg5136 (2024).

1019 28. Telley, L. *et al.* Sequential transcriptional waves direct the differentiation of newborn
1020 neurons in the mouse neocortex. *Science (1979).* **351**, 1443–1446 (2016).

1021 29. Liodis, P. *et al.* Lhx6 activity is required for the normal migration and specification of
1022 cortical interneuron subtypes. *Journal of Neuroscience* **27**, 3078–3089 (2007).

1023 30. Miyoshi, G. *et al.* Prox1 regulates the subtype-specific development of caudal ganglionic
1024 eminence-derived GABAergic cortical interneurons. *Journal of Neuroscience* **35**, 12869–
1025 12889 (2015).

1026 31. Tremblay, R., Lee, S. & Rudy, B. GABAergic interneurons in the neocortex: from cellular
1027 properties to circuits. *Neuron* **91**, 260–292 (2016).

1028 32. Cardin, J. A. Inhibitory interneurons regulate temporal precision and correlations in
1029 cortical circuits. *Trends Neurosci.* **41**, 689–700 (2018).

1030 33. Huang, Z. J. & Paul, A. The diversity of GABAergic neurons and neural communication
1031 elements. *Nat. Rev. Neurosci.* **20**, 563–572 (2019).

1032 34. Liakath-Ali, K. & Südhof, T. C. The Perils of Navigating Activity-Dependent Alternative
1033 Splicing of Neurexins. Front. Mol. Neurosci. 14, 659681. Preprint at (2021).

1034 35. Baxter, P. S., Dando, O. & Hardingham, G. E. Differential splicing choices made by
1035 neurons and astrocytes and their importance when investigating signal-dependent
1036 alternative splicing in neural cells. *Front. Mol. Neurosci.* **16**, 1214439 (2023).

1037 36. Ramos, S. I. *et al.* An atlas of late prenatal human neurodevelopment resolved by single-
1038 nucleus transcriptomics. *Nat. Commun.* **13**, 7671 (2022).

1039 37. Wang, L. *et al.* Molecular and cellular dynamics of the developing human neocortex.
1040 *Nature* 1–10 (2025).

1041 38. Zhu, K. *et al.* Multi-omic profiling of the developing human cerebral cortex at the single-
1042 cell level. *Sci. Adv.* **9**, eadg3754 (2023).

1043 39. Eze, U. C., Bhaduri, A., Haeussler, M., Nowakowski, T. J. & Kriegstein, A. R. Single-cell
1044 atlas of early human brain development highlights heterogeneity of human neuroepithelial
1045 cells and early radial glia. *Nat. Neurosci.* **24**, 584–594 (2021).

1046 40. Sebastian, R. *et al.* Schizophrenia-associated NRXN1 deletions induce developmental-
1047 timing-and cell-type-specific vulnerabilities in human brain organoids. *Nat. Commun.* **14**,
1048 3770 (2023).

1049 41. Birey, F. *et al.* Assembly of functionally integrated human forebrain spheroids. *Nature*
1050 **545**, 54–59 (2017).

1051 42. Trujillo, C. A. *et al.* Complex oscillatory waves emerging from cortical organoids model
1052 early human brain network development. *Cell Stem Cell* **25**, 558–569 (2019).

1053 43. Fair, S. R. *et al.* Electrophysiological maturation of cerebral organoids correlates with
1054 dynamic morphological and cellular development. *Stem Cell Reports* **15**, 855–868 (2020).

1055 44. Park, Y. *et al.* Modulation of neuronal activity in cortical organoids with bioelectronic
1056 delivery of ions and neurotransmitters. *Cell Reports Methods* **4**, (2024).

1057 45. Matsunami, N. *et al.* Identification of rare recurrent copy number variants in high-risk
1058 autism families and their prevalence in a large ASD population. *PLoS One* **8**, e52239
1059 (2013).

1060 46. Kim, H.-G. *et al.* Disruption of neurexin 1 associated with autism spectrum disorder. *The*
1061 *American Journal of Human Genetics* **82**, 199–207 (2008).

1062 47. Kozareva, V. *et al.* A transcriptomic atlas of mouse cerebellar cortex comprehensively
1063 defines cell types. *Nature* **598**, 214–219 (2021).

1064 48. Kim, J. & Augustine, G. J. Molecular layer interneurons: key elements of cerebellar
1065 network computation and behavior. *Neuroscience* **462**, 22–35 (2021).

1066 49. Brown, A. M. *et al.* Molecular layer interneurons shape the spike activity of cerebellar
1067 Purkinje cells. *Sci. Rep.* **9**, 1742 (2019).

1068 50. Wisden, W., Murray, A. J., McClure, C. J. & Wulff, P. Studying cerebellar circuits by
1069 remote control of selected neuronal types with GABA-A receptors. *Front. Mol. Neurosci.*
1070 **2**, 808 (2009).

1071 51. Brunet de Courssou, J.-B., Durr, A., Adams, D., Corvol, J.-C. & Mariani, L.-L. Antisense
1072 therapies in neurological diseases. *Brain* **145**, 816–831 (2022).

1073 52. Ottesen, E. W., Luo, D., Singh, N. N. & Singh, R. N. High concentration of an ISS-N1-
1074 targeting antisense oligonucleotide causes massive perturbation of the transcriptome. *Int.*
1075 *J. Mol. Sci.* **22**, 8378 (2021).

1076 53. Mortberg, M. A. *et al.* A single-cell map of antisense oligonucleotide activity in the brain.
1077 *Nucleic Acids Res.* **51**, 7109–7124 (2023).

1078 54. Buijsen, R. A. M. *et al.* Calcium-enhanced medium-based delivery of splice modulating
1079 antisense oligonucleotides in 2D and 3D hiPSC-derived neuronal models. *Biomedicines*
1080 **12**, 1933 (2024).

1081 55. Hjelmgren, L. *et al.* Dysregulation of the DNA damage response by phosphorothioate
1082 antisense oligonucleotides. *Nat. Commun.* (2026).

1083 56. Lim, L., Mi, D., Llorca, A. & Marín, O. Development and functional diversification of
1084 cortical interneurons. *Neuron* **100**, 294–313 (2018).

1085 57. Nguyen, T.-M. *et al.* An alternative splicing switch shapes neurexin repertoires in principal
1086 neurons versus interneurons in the mouse hippocampus. *Elife* **5**, e22757 (2016).

1087 58. Biswas, M. S., Roy, S. K., Hasan, R. & Pk, M. M. U. The crucial role of the cerebellum in
1088 autism spectrum disorder: neuroimaging, neurobiological, and anatomical insights. *Health*
1089 *Sci. Rep.* **7**, e2233 (2024).

1090 59. van der Heijden, M. E., Gill, J. S. & Sillitoe, R. V. Abnormal cerebellar development in
1091 autism spectrum disorders. *Dev. Neurosci.* **43**, 181–190 (2021).

1092 60. D'Mello, A. M. & Stoodley, C. J. Cerebro-cerebellar circuits in autism spectrum disorder.
1093 *Front. Neurosci.* **9**, 408 (2015).

1094 61. Peng, H. *et al.* Single-cell Rapid Capture Hybridization sequencing reliably detects
1095 isoform usage and coding mutations in targeted genes. *Genome Res.* **35**, 942–955
1096 (2025).

1097 62. Richter, D. *et al.* The age of the hominin fossils from Jebel Irhoud, Morocco, and the
1098 origins of the Middle Stone Age. *Nature* **546**, 293–296 (2017).

1099 63. Bhaduri, A. *et al.* Cell stress in cortical organoids impairs molecular subtype specification.
1100 *Nature* **578**, 142–148 (2020).

1101 64. Lowther, C. *et al.* Molecular characterization of NRXN1 deletions from 19,263 clinical
1102 microarray cases identifies exons important for neurodevelopmental disease expression.
1103 *Genetics in Medicine* **19**, 53–61 (2017).

1104 65. Koopmans, F. *et al.* SynGO: an evidence-based, expert-curated knowledge base for the
1105 synapse. *Neuron* **103**, 217–234 (2019).

1106 66. Sloan, S. A., Andersen, J., Pașca, A. M., Birey, F. & Pașca, S. P. Generation and
1107 assembly of human brain region–specific three-dimensional cultures. *Nat. Protoc.* **13**,
1108 2062–2085 (2018).

1109 67. Chen, X. *et al.* Antisense oligonucleotide therapeutic approach for Timothy syndrome.
1110 *Nature* **628**, 818–825 (2024).

1111 68. Hao, Y. *et al.* Dictionary learning for integrative, multimodal and scalable single-cell
1112 analysis. *Nat. Biotechnol.* **42**, 293–304 (2024).

1113 69. McGinnis, C. S., Murrow, L. M. & Gartner, Z. J. DoubletFinder: doublet detection in
1114 single-cell RNA sequencing data using artificial nearest neighbors. *Cell Syst.* **8**, 329–337
1115 (2019).

1116 70. Prjibelski, A. D. *et al.* Accurate isoform discovery with IsoQuant using long reads. *Nat.*
1117 *Biotechnol.* **41**, 915–918 (2023).

1118 71. Li, Y. I. *et al.* Annotation-free quantification of RNA splicing using LeafCutter. *Nat. Genet.*
1119 **50**, 151–158 (2018).

1120 72. You, Y. *et al.* Identification of cell barcodes from long-read single-cell RNA-seq with
1121 BLAZE. *Genome Biol.* **24**, 66 (2023).

1122 73. Li, H. *et al.* Improving gene isoform quantification with miniQuant. *Nat. Biotechnol.* 1–13
1123 (2025).

1124 74. Joglekar, A. *et al.* Single-cell long-read sequencing-based mapping reveals specialized
1125 splicing patterns in developing and adult mouse and human brain. *Nat. Neurosci.* **27**,
1126 1051–1063 (2024).

1127

An Integrated Targeting Strategy Reveals Cell-Type Atlas of *NRXN1* Isoforms Across Human Brain Development and Genetic Backgrounds

a

Percentage of *NRXN1* reads by cell type with/ without Capture-seq

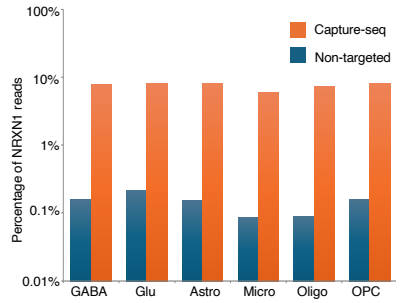

Fold enrichment of *NRXN1* reads by cell type

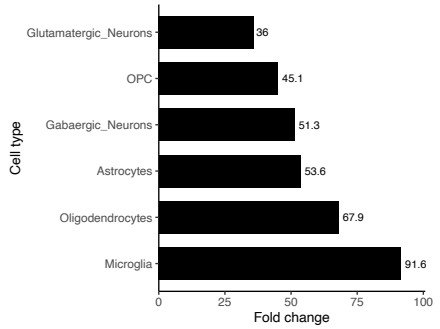

b

Workflow for comprehensive study of cell-type specific *NRXN1* isoforms

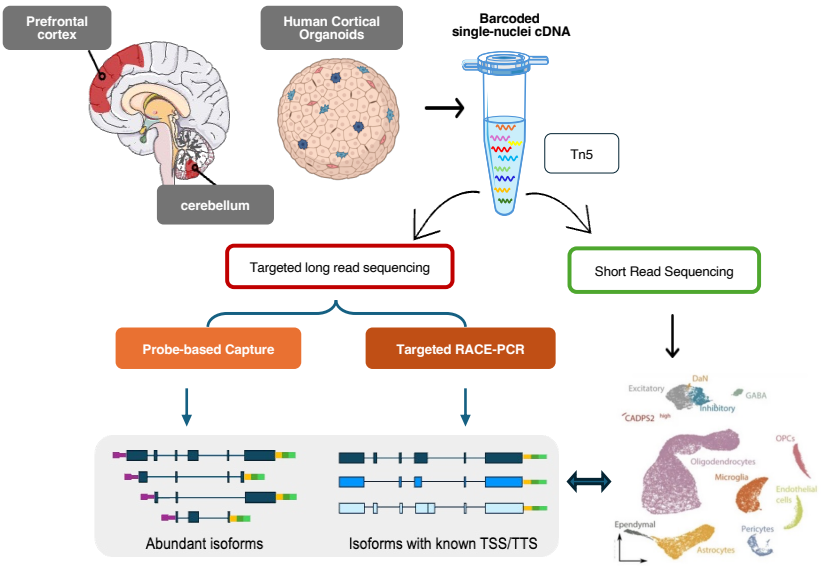

c

Cell type–resolved NRXN1 isoforms identified across samples by single-cell long-read Capture-seq

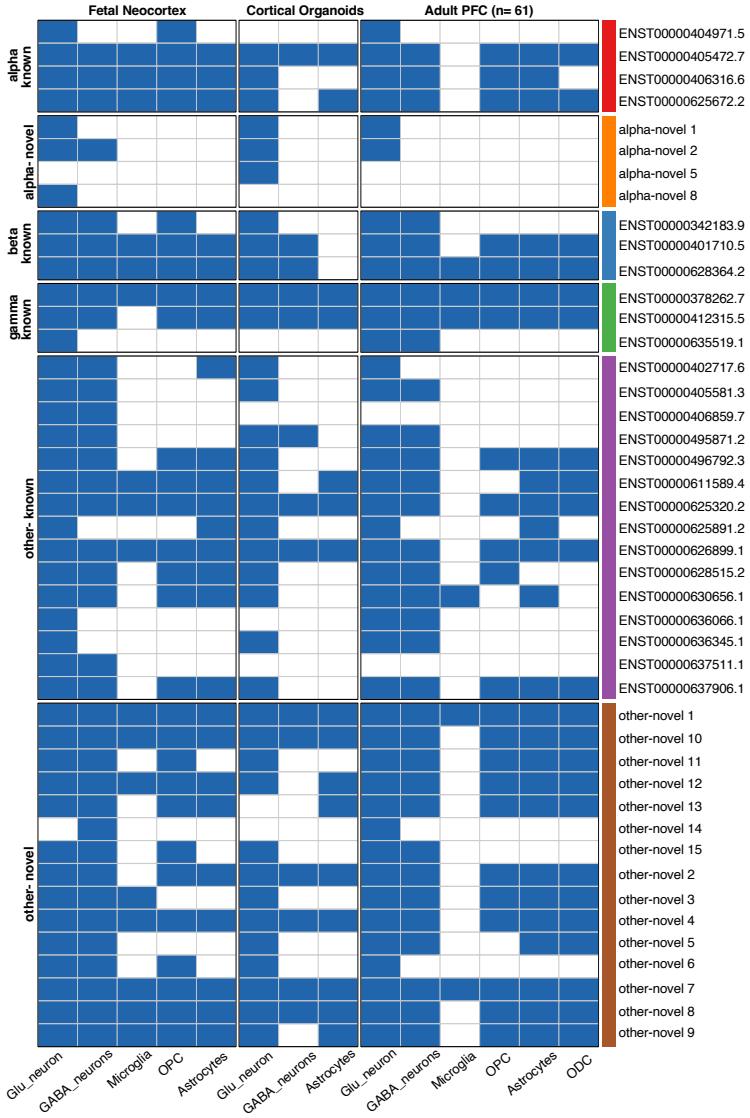

d

***NRXN1* splicing profiles in glutamatergic and GABAergic neuron classes across samples**

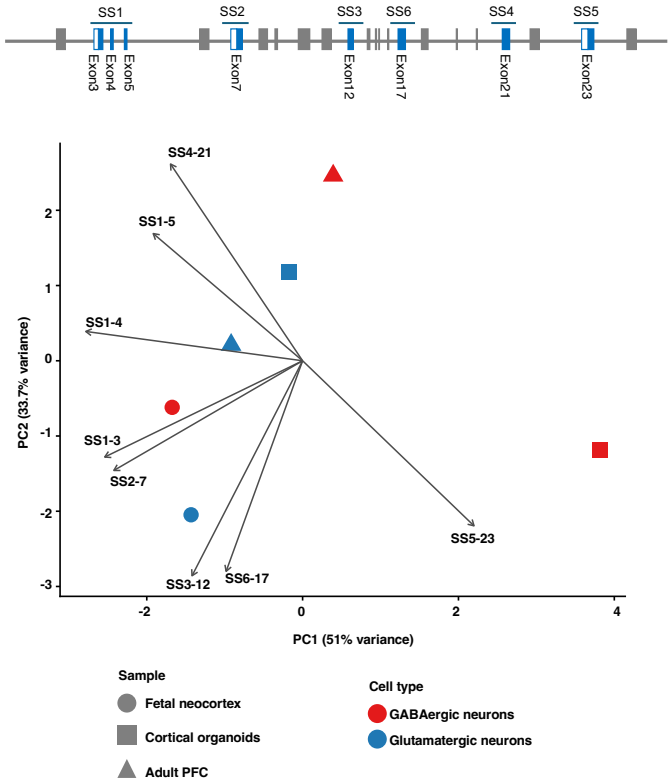

NRXN1 expression repertoires exhibit distinct splicing patterns across cell types in human brains

a Resolve cell-type specific *NRXN1* isoforms by probe-based long-read Capture-seq

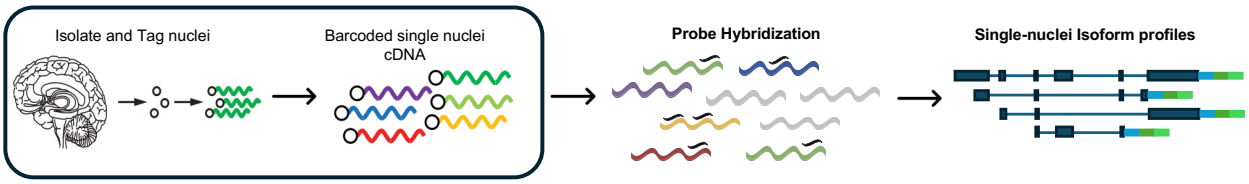

b UMAP visualization of cell types in the PFC of adult brains

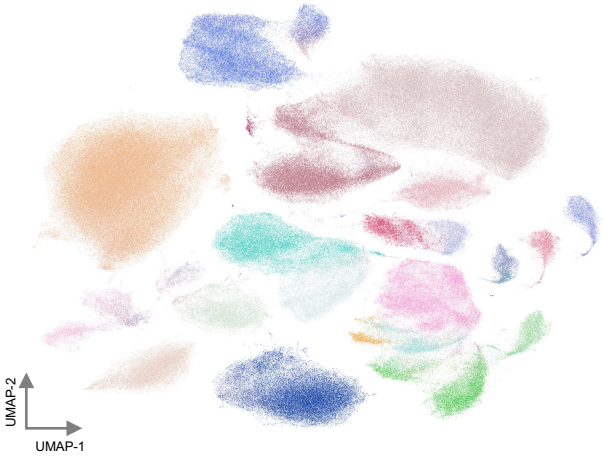

d PCA plot of *NRXN1* AS events across cell types

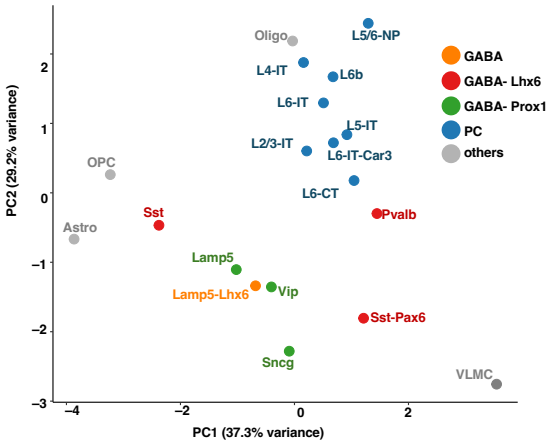

c Cell-type-specific *NRXN1* splicing patterns of SS1-6 revealed by long-read Capture-seq

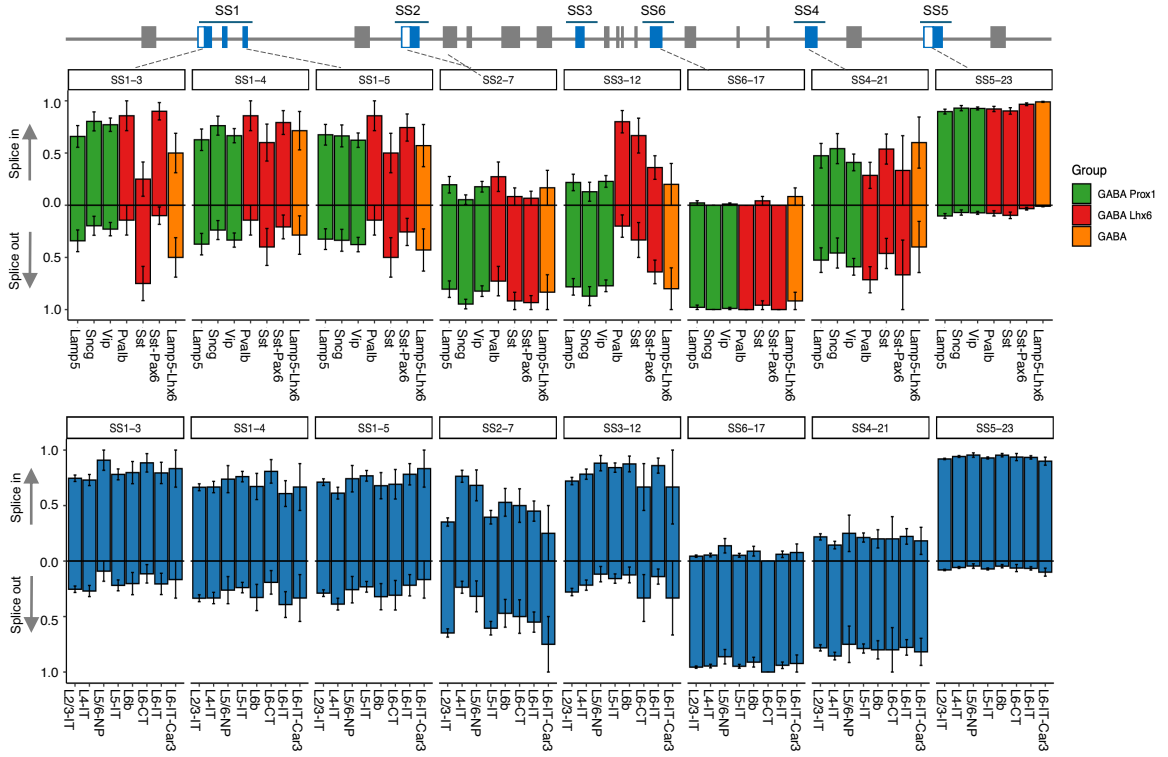

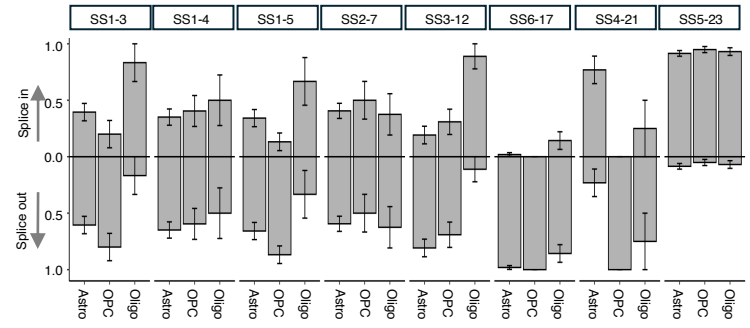

e Exon Inclusion difference: GABA VS Glu

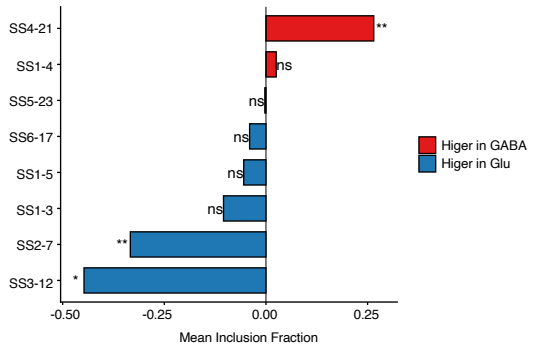

NRXN1 splicing profiles remain consistent across cells sharing a neurogenic origin during neural maturation

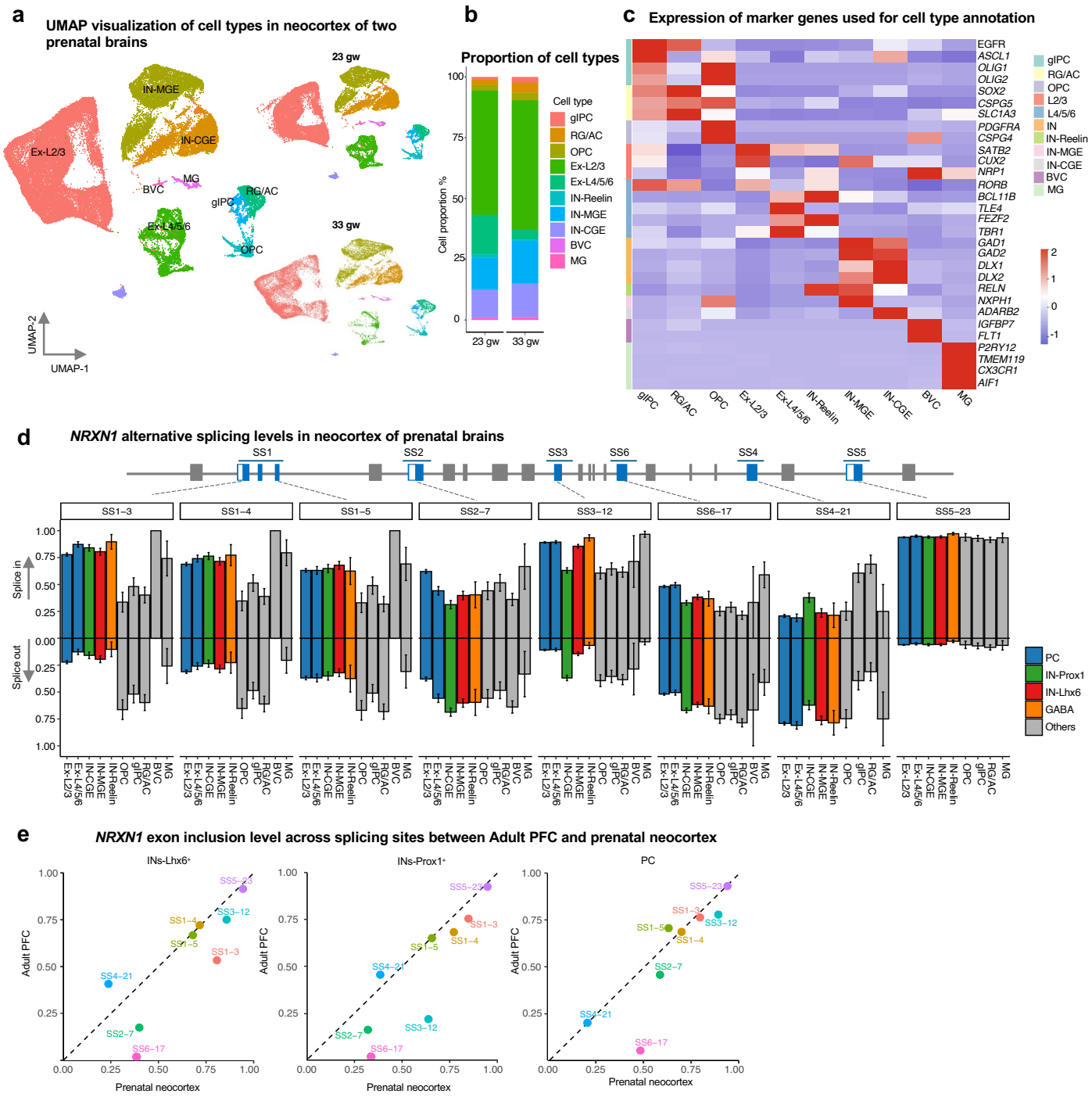

NRXN1$^{+/-}$ hCOs splicing profiles recapitulate developmental and mature features and identify cell types expressing the mutant isoforms

a UMAP visualization of cell types in organoids

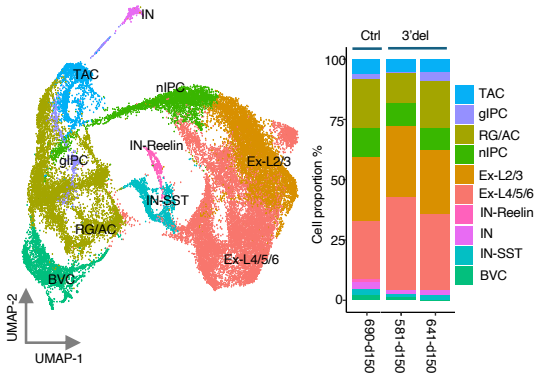

b Expression of marker genes used for cell type annotation

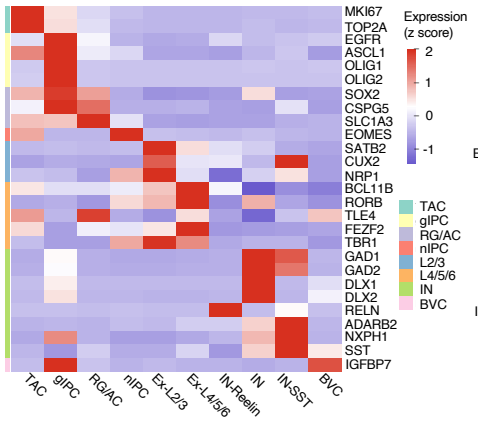

c Cell type enrichment for cells in 3'-del organoids vs control

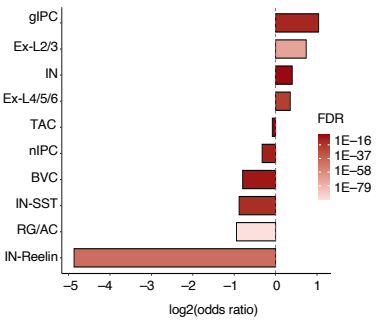

d *NRXN1* Alternative splicing levels in control organoids (upper) and 3'-del organoids (lower)

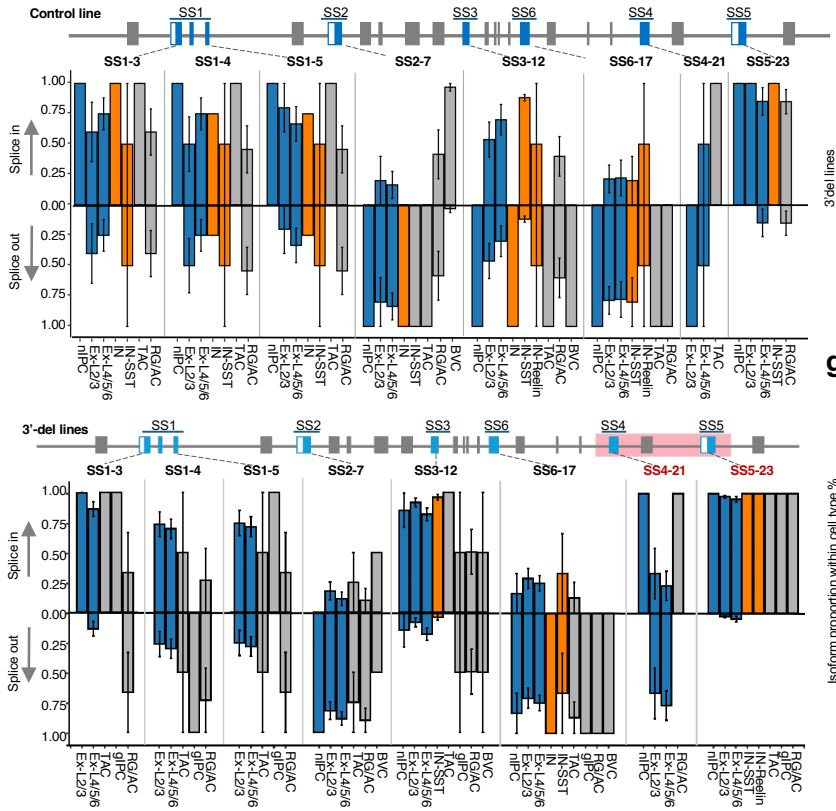

e *NRXN1* exon inclusion level across splicing sites between between 3'del and control lines

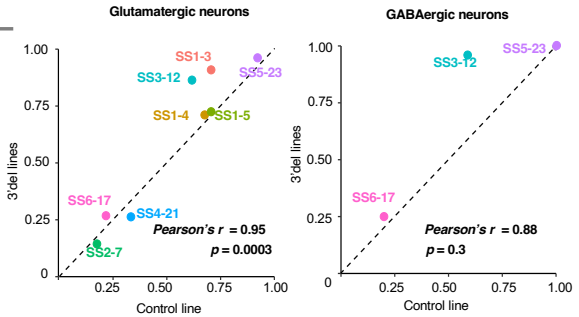

g Composition of *NRXN1* isoforms within each cell type

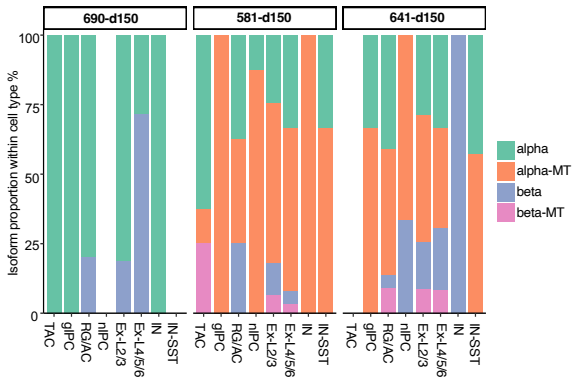

f *NRXN1α* isoforms identified from organoids by Long-range RACE-seq

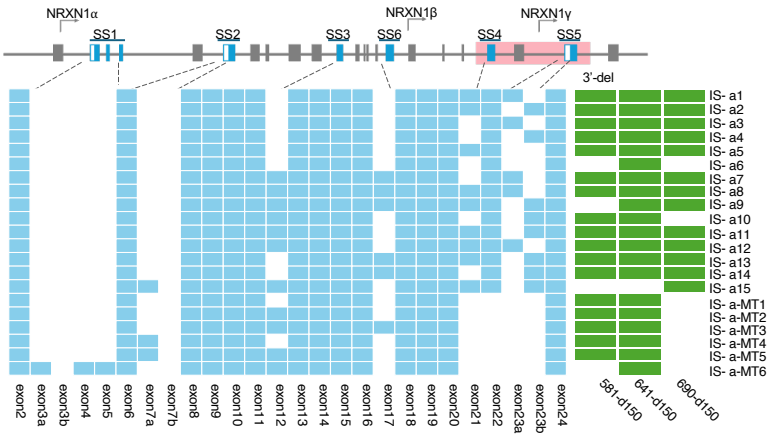

h Exon inclusion levels at splice sites (SS1–SS6) for GABA-IN, Glu-EX, and RG/AC across hCOs, fetal neocortex, and adult PFC

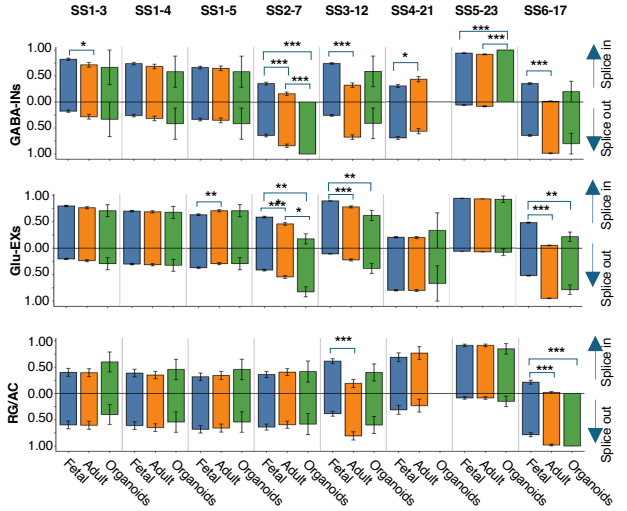

A patient-specific *exonic* deletion drives cell-type–specific enrichment of mutant *NRXN1* isoforms in the ASD cerebellum

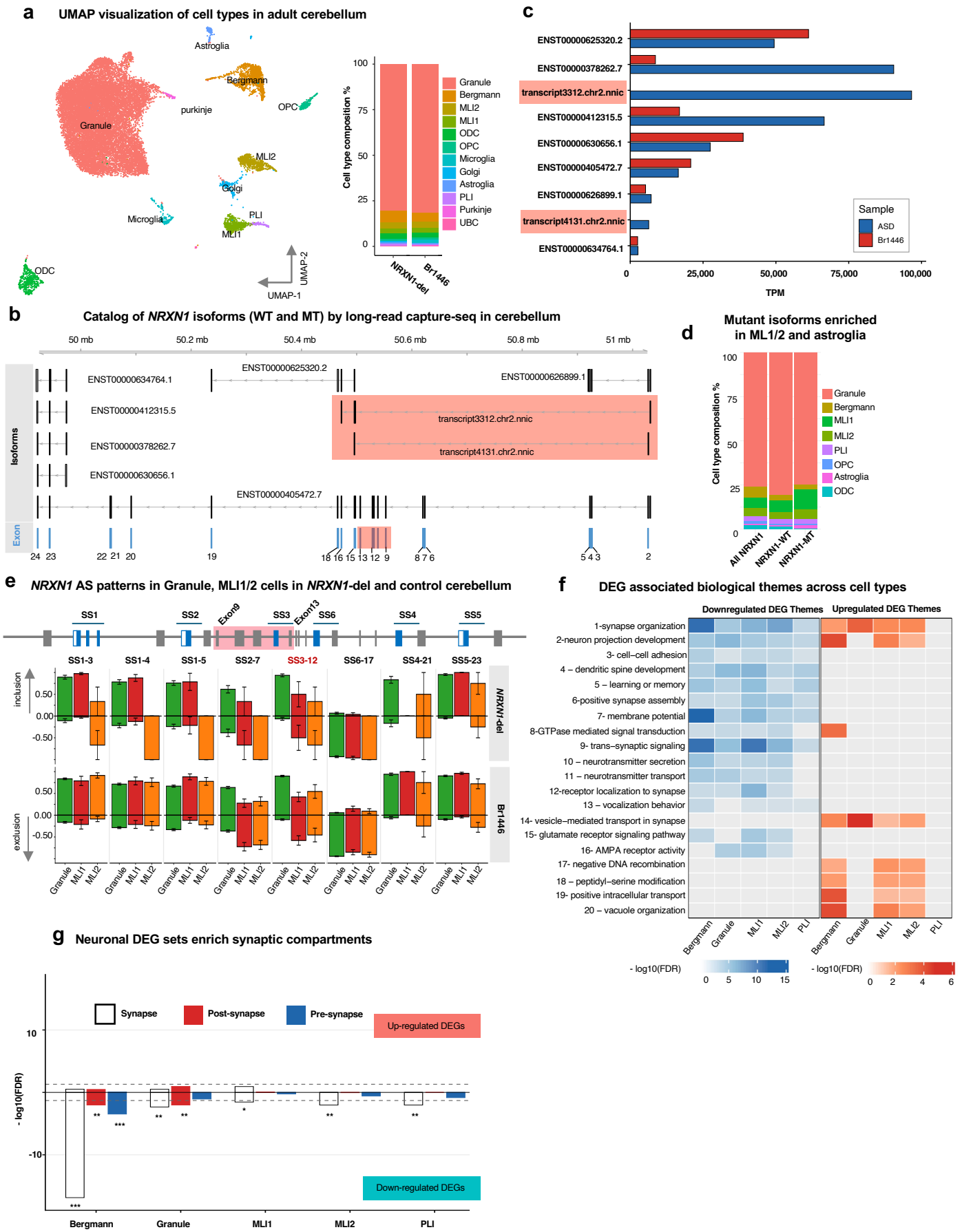
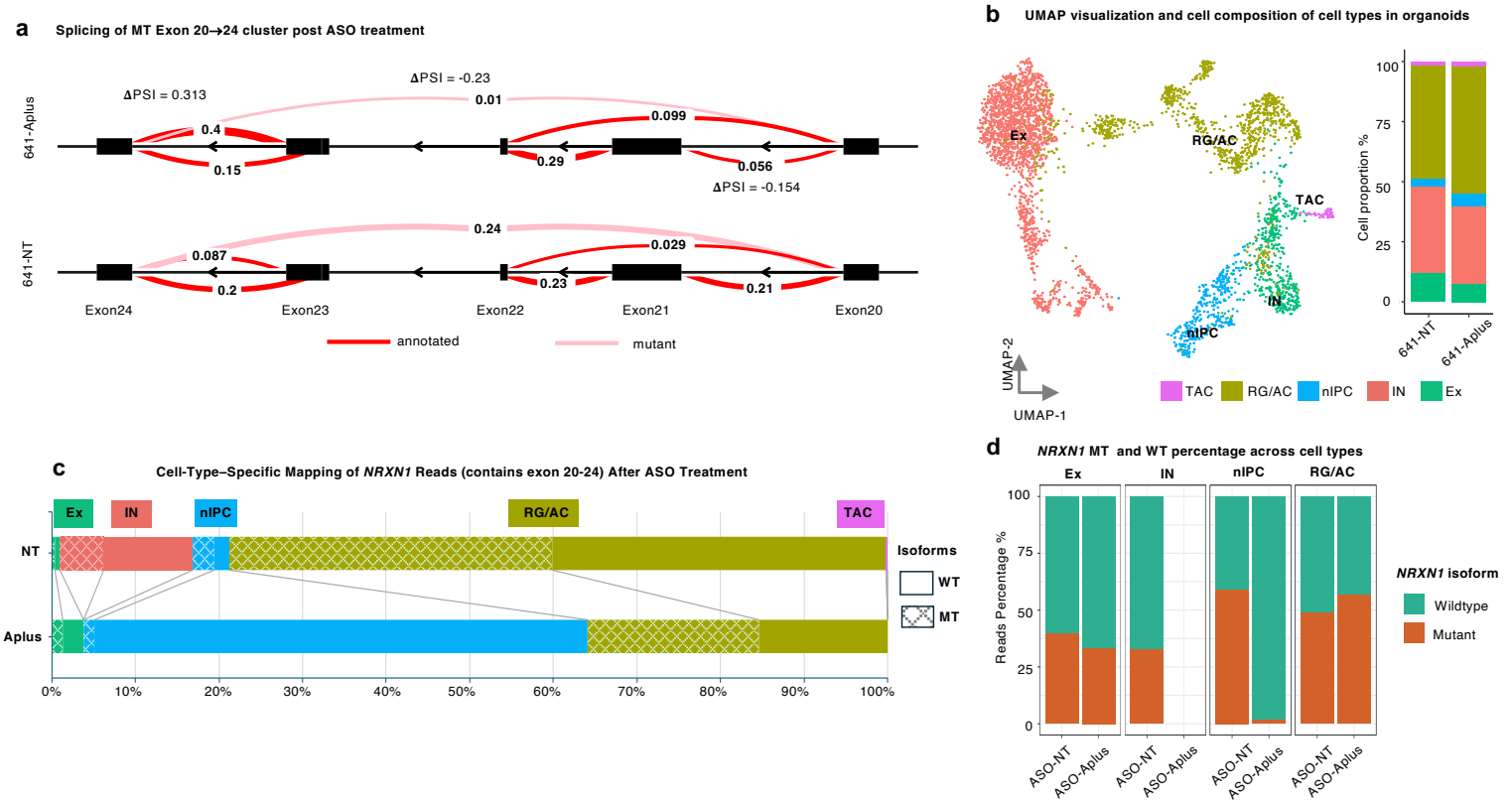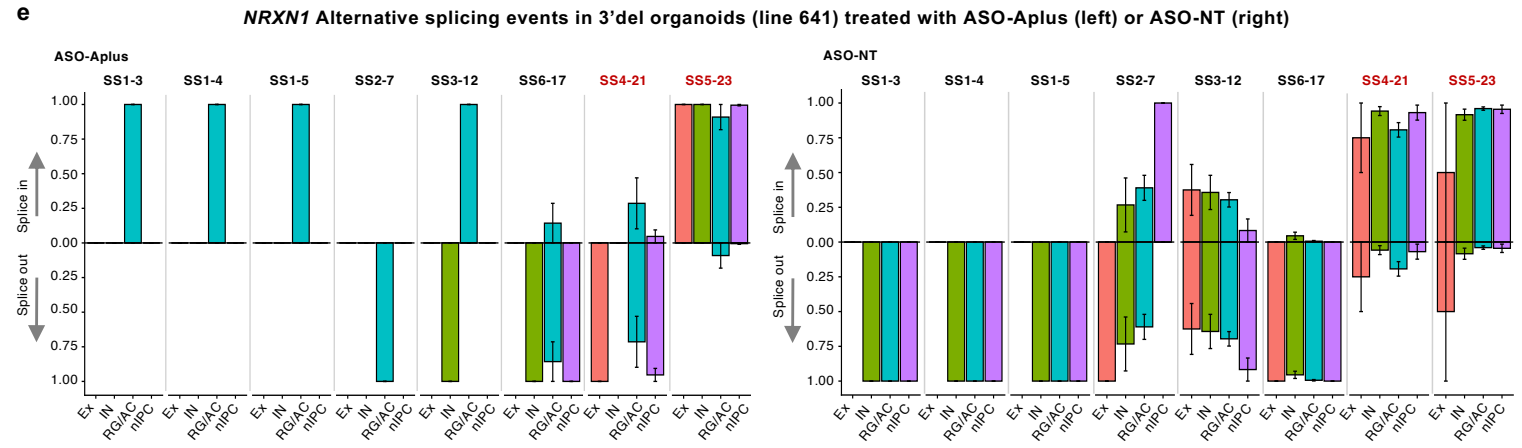
Evaluation framework for cell-type–resolved ASO inhibition of GOF *NRXN1* isoforms in cortical organoids